

May 2020

Design and Modal Analysis of an Ultra-wideband Receiver for Green Bank Observatory

Alyssa Bulatek
Macalester College, alyssabulatek@gmail.com

Follow this and additional works at: <https://digitalcommons.macalester.edu/mjpa>



Part of the [Astrophysics and Astronomy Commons](#), and the [Physics Commons](#)

Recommended Citation

Bulatek, Alyssa (2020) "Design and Modal Analysis of an Ultra-wideband Receiver for Green Bank Observatory," *Macalester Journal of Physics and Astronomy*. Vol. 8: Iss. 1, Article 3.
Available at: <https://digitalcommons.macalester.edu/mjpa/vol8/iss1/3>

This Honors Project - Open Access is brought to you for free and open access by the Physics and Astronomy Department at DigitalCommons@Macalester College. It has been accepted for inclusion in Macalester Journal of Physics and Astronomy by an authorized editor of DigitalCommons@Macalester College. For more information, please contact scholarpub@macalester.edu.

Design and Modal Analysis of an Ultra-wideband Receiver for Green Bank Observatory

Abstract

The next generation of radio receivers for astronomy will be marked by tenfold improvements in sensitivity. These sensitive receivers will be useful for the detection of broadband fast radio bursts and other transients as well as the efficient discovery of radio recombination lines among many other scientific pursuits. One contribution to these improvements is an increase to decade receiver bandwidths. The Green Bank Observatory (GBO) is currently in the process of fabricating a new ultra-wideband (UWB; 0.7 to 4.2 GHz) receiver for the Green Bank Telescope (GBT). The UWB receiver will be used by the North American Nanohertz Observatory for Gravitational Waves (NANOGrav) to perform pulsar timing experiments using the GBT with greater sensitivity than before. The design of the receiver features a quad-ridged, flared feed horn and utilizes a corrugated skirt and a quartz spear to extend the receiver's bandwidth to 6:1. Through modeling and performance simulation, we find the predicted efficiency of the receiver to be around 60–70% at lower frequencies and above 50% at higher frequencies. The S_{11} values for the UWB receiver are better than -10 dB across the entire bandwidth, and performance is only predicted to degrade slightly at 2.8 GHz with the inclusion of a waveguide window.

In an effort to determine the potential cause of reduced efficiency as a function of frequency, we perform an analysis of waveguide mode excitation to determine the concentration of higher-order mode excitation in the aperture of the receiver. Preliminary results suggest that higher-order mode (i.e. TM_{12} and TM_{13}) excitation is present at higher frequencies, but we cannot conclude that it is the sole cause of reduced feed efficiency at those frequencies.

Keywords

ultra-wideband, receiver, pulsar, astronomy

Cover Page Footnote

This project was funded by the National Science Foundation through the Research Experience for Undergraduates program at the Green Bank Observatory. The Green Bank Observatory is a facility of the National Science Foundation operated under cooperative agreement by Associated Universities, Inc.

MACALESTER COLLEGE

Design and Modal Analysis of an
Ultra-wideband Receiver for
Green Bank Observatory

by

Alyssa Bulatek

in the

Department of Physics and Astronomy

Advisor: John Cannon

May 2020

MACALESTER COLLEGE

Abstract

Department of Physics and Astronomy

by Alyssa Bulatek

The next generation of radio receivers for astronomy will be marked by tenfold improvements in sensitivity. These sensitive receivers will be useful for the detection of broadband fast radio bursts and other transients as well as the efficient discovery of radio recombination lines among many other scientific pursuits. One contribution to these improvements is an increase to decade receiver bandwidths. The Green Bank Observatory (GBO) is currently in the process of fabricating a new ultra-wideband (UWB; 0.7 to 4.2 GHz) receiver for the Green Bank Telescope (GBT). The UWB receiver will be used by the North American Nanohertz Observatory for Gravitational Waves (NANOGrav) to perform pulsar timing experiments using the GBT with greater sensitivity than before. The design of the receiver features a quad-ridged, flared feed horn and utilizes a corrugated skirt and a quartz spear to extend the receiver's bandwidth to 6:1. Through modeling and performance simulation, we find the predicted efficiency of the receiver to be around 60–70% at lower frequencies and above 50% at higher frequencies. The S_{11} values for the UWB receiver are better than -10 dB across the entire bandwidth, and performance is only predicted to degrade slightly at 2.8 GHz with the inclusion of a waveguide window.

In an effort to determine the potential cause of reduced efficiency as a function of frequency, we perform an analysis of waveguide mode excitation to determine the concentration of higher-order mode excitation in the aperture of the receiver. Preliminary results suggest that higher-order mode (i.e. TM_{12} and TM_{13}) excitation is present at higher frequencies, but we cannot conclude that it is the sole cause of reduced feed efficiency at those frequencies.

Acknowledgements

I would like to begin by thanking my thesis committee, consisting of Steve White, John Cannon, and James Heyman, for providing thoughtful comments on drafts of my thesis and challenging me to do my best.

Steve: I am very thankful for your guidance and expertise along the way (and for lending me a bike over the summer). Even when we were trying to troubleshoot code remotely, you were always patient and willing to work with me at the pace I was working at, and for that, I am so grateful.

John: You have always gone the extra mile to support me, and I am very thankful for that. Thank you for never letting me give up. Thank you for telling me the floral suitcase story when I needed it most. Thank you for always finding the excitement in your day-to-day work. You are the best role model a young astronomer could ask for, and I will never forget you.

Professor Heyman: Thank you for letting me make mistakes in so many of your classes and labs throughout the years. Modern Physics was really tough for me, but you are one of the most patient professors I have ever had. You were always willing to explain and re-explain concepts at office hours, and that made me a lot less scared of asking questions. Thank you for your generosity and kindness.

Many thanks are also due to Bob Simon and Ryan Lynch at Green Bank Observatory for helping me with parts of this project that I was initially unfamiliar with (waveguide windows and pulsar timing respectively). Thank you to Sivasankaran Srikanth at the Central Development Laboratory for your assistance with the reflector edge angle calculations, and thank you to Lisa Locke (now at JPL) for your help with getting started with CST.

I would like to extend a huge thank you to the faculty and staff in the Physics and Astronomy department at Macalester for four years of friendship and support. Thank you for teaching me what I know and letting me explore what I love about learning. I would also like to thank the other students in the department, especially the seniors, for being my friends and for making up a great school-family to be part of.

I would not have been able to complete this project without the support of my previous research advisors, who will still write letters of reference for me if I ask them to (thank you!). Craig McMurtry, Judy Pipher, and Kevin Flaherty: you are shining examples of amazing researchers who I have been so glad to get to know. Thank you for letting me learn about research in your labs and offices.

I would especially like to thank my dear friends, Lilly, Greta, and James, for putting up with me during college and for watching so many movies. You are really the best friends a kid could ask for.

Special thanks to the fellow residents of the Hannah House during summer 2019, who proved that one can survive three months without a cell phone. Thank you for driving me to the grocery store and saying good things about the mediocre food I made.

I should also thank my mom and dad for their support throughout my entire life. I am very fortunate to have parents as cool as you.

Contents

Abstract	i
Acknowledgements	ii
List of Figures	vi
List of Tables	vii
1 Introduction	1
1.1 Overview	1
1.2 Recent Ultra-wideband Technology	2
1.3 Motivation	3
2 Background	6
2.1 Pulsars	6
2.2 Pulsar Timing	8
2.3 Waveguides	9
2.4 Radio Receivers	11
3 UWB Receiver Efficiency	13
3.1 Receiver Specifications and Models	13
3.1.1 Receiver Models	13
3.2 Receiver Efficiency	15
3.2.1 Spillover Efficiency	16
3.2.2 Illumination Efficiency	18
3.2.3 Cross-polarization and Phase Efficiencies	19
3.3 Efficiency Analysis	19
3.3.1 Spillover Temperature Correction	27
3.3.2 Reflector Edge Angles	29
4 UWB Receiver Window	30
4.1 Waveguide Windows	30
4.2 Modeling Window Circuit Properties	31
4.3 Measuring Window Strength	34
5 UWB Receiver Modal Excitation	37
5.1 Motivation for Mode Analysis	37

<i>Contents</i>	v
5.2 Circular Aperture Technique	37
5.3 Mode Analysis Results	39
6 Conclusions and Future Work	43
Bibliography	45

List of Figures

1.1	Gravitational wave spectrum from Moore et al. (2019)	2
1.2	Pulsar signal undergoing dispersion from Condon & Ransom (2016)	5
2.1	Pulsar diagram from Lorimer & Kramer (2005)	7
2.2	Rectangular waveguide from Griffiths (2013)	10
2.3	UWB receiver three-dimensional far-field pattern	12
3.1	UWB receiver feed horn model (perspective view)	14
3.2	UWB receiver feed horn model (side view)	15
3.3	Depiction of spillover radiation reaching a receiver's beam	17
3.4	Cut angle diagram	20
3.5	UWB receiver (sub-)efficiency for Model A, E plane	21
3.6	UWB receiver (sub-)efficiency for Model A, D plane	21
3.7	UWB receiver (sub-)efficiency for Model A, H plane	22
3.8	UWB receiver (sub-)efficiency for Model B, E plane	23
3.9	UWB receiver (sub-)efficiency for Model B, D plane	23
3.10	UWB receiver (sub-)efficiency for Model B, H plane	24
3.11	UWB receiver (sub-)efficiency for Model C, E plane	24
3.12	UWB receiver (sub-)efficiency for Model C, D plane	25
3.13	UWB receiver (sub-)efficiency for Model C, H plane	25
3.14	UWB receiver (sub-)efficiency for Model D, E plane	26
3.15	UWB receiver (sub-)efficiency for Model D, D plane	26
3.16	UWB receiver (sub-)efficiency for Model D, H plane	27
4.1	Receiver with window at GBT prime focus	31
4.2	UWB receiver feed horn model with window in aperture (perspective view)	32
4.3	UWB receiver feed horn model with window in aperture (side view)	32
4.4	UWB receiver feed horn model with smaller window	33
4.5	UWB receiver simulated S_{11} parameters, no window in model	34
4.6	UWB receiver simulated S_{11} parameters, window in model	35
4.7	UWB receiver waveguide window prototyping process	36
5.1	UWB receiver modal analysis at aperture (Model C)	40
5.2	UWB receiver modal analysis at aperture (Model D)	42

List of Tables

3.1	UWB receiver model iterations	15
3.2	Edge angles of the GBT reflector dish	29

CHAPTER 1: Introduction

1.1 Overview

This thesis summarizes the design and development process of a new ultra-wideband (UWB) radio receiver for the Green Bank Telescope. This sensitive receiver will be used by the North American Nanohertz Observatory for Gravitational Waves (NANOGrav) to time pulsars with about twice as much accuracy as previous observations in the hopes of detecting gravitational waves. Though pulsar-dependent, these increases in timing precision are results of an increase in observing time per pulsar as well as an increase in bandwidth for each observation (Ryan Lynch, personal correspondence). If successful, pulsar-timing-based gravitational wave detection would expand our knowledge of the gravitational wave spectrum, complementing ground-based detections reported by [Abbott et al. \(2016\)](#) and many other works. Nanohertz-frequency gravitational waves probe different astronomical processes than higher-frequency gravitational waves, as shown in [Figure 1.1](#).

We present a comprehensive analysis of the predicted efficiency of the UWB receiver across its bandwidth which shows that the receiver meets specified design goals. We also present an analysis of the receiver's circuit characteristics, which are necessary to analyze due to the receiver's large size. We also perform a waveguide mode breakdown in the aperture of the receiver to determine causes of reduced efficiency as a function of frequency.

This chapter summarizes recent ultra-wideband receiver technology and describes the motivation for the project. [Chapter 2](#) provides additional background information on pulsar timing and radio receiver technology, which are not often discussed a standard undergraduate physics curriculum. [Chapter 3](#) describes the standard sources of reduced efficiency for the UWB receiver and presents its predicted efficiency. In [Chapter 4](#), we describe a crucial component of the cryogenic system for the receiver and analyze its effect on the receiver's circuit properties. The mode excitation analysis for the UWB receiver is presented in [Chapter 5](#). Conclusions

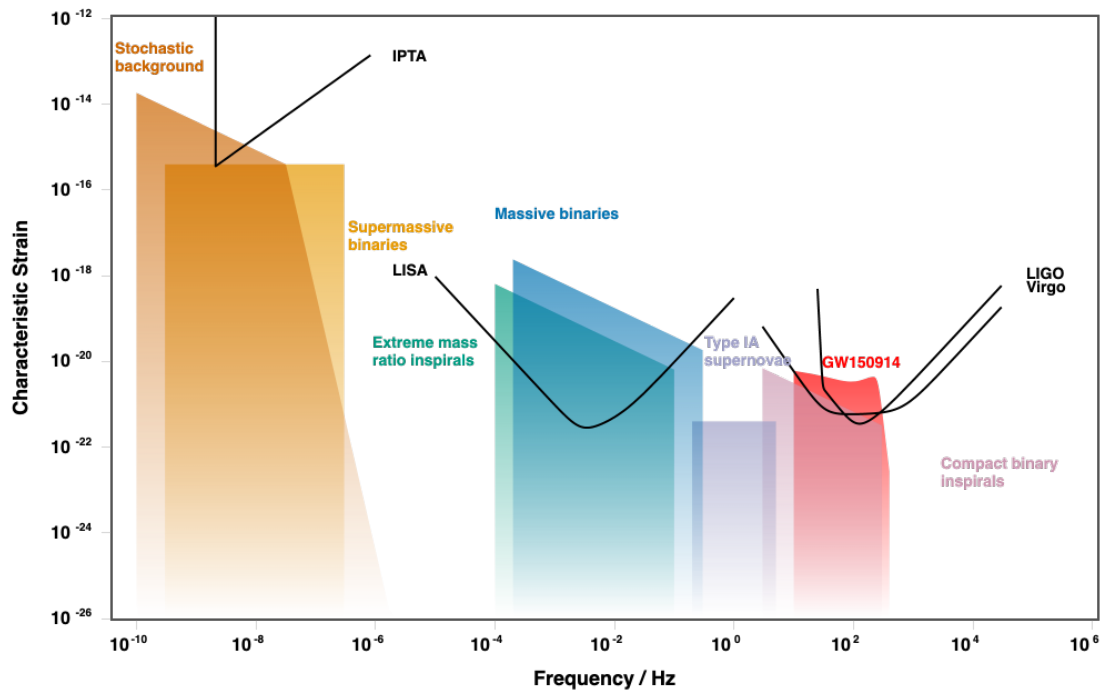


FIGURE 1.1: Sources of gravitational waves and the detectors capable of detecting them. The International Pulsar Timing Array (IPTA) is used by NANOGrav. The Laser Interferometer Space Antenna (LISA) mission will be the first space-based gravitational wave observatory. LISA Pathfinder results were first published in [Armano et al. \(2016\)](#). The Laser Interferometer Gravitational-Wave Observatory (LIGO) and Virgo are ground-based laser interferometers in the United States and Italy respectively ([Abbott et al. 2016](#)). Created using [Moore et al. \(2019\)](#).

made from the project as well as a discussion of future work are presented in Chapter 6.

1.2 Recent Ultra-wideband Technology

Wideband receiver technology is the future of radio astronomy for several reasons. The scientific benefits of wideband receivers are not only limited to pulsar observations, but also extend to very long baseline interferometry (VLBI) experiments and the search for spectral lines with unknown redshifts. There are also applications in array technology, where many different antennas need identical

components and large-bandwidth receivers reduce the cost per antenna because one receiver is needed instead of several (Akgiray 2013).

An ultra-wideband feed horn has been designed and prototyped for the Parkes radio telescope in Australia (Dunning et al. 2015). This receiver's bandwidth (0.7 to 4.2 GHz) has been optimized for pulsar timing and it incorporates a differential feed which can support observation at two linear polarizations simultaneously. In the northern hemisphere, several wideband feeds were proposed for construction at Arecibo Observatory in Puerto Rico in an Astro2020 White Paper (Roshi et al. 2019). Wideband receivers will reduce the number of receivers necessary to cover the bandwidth of the telescope at Arecibo and provide increased sensitivity for broadband science targets like pulsars and ultra-cool dwarfs (Roshi et al. 2019). Many large telescopes around the world are harnessing their unique capabilities by starting to build ultra-wideband receivers for radio astronomy applications.

1.3 Motivation

The Robert C. Byrd Green Bank Telescope (GBT) is one of two telescopes used for pulsar timing observations for NANOGrav along with the William E. Gordon Telescope at Arecibo Observatory. Currently, NANOGrav uses two different receivers on the GBT to observe pulsars. One is centered at 800 MHz with a bandwidth of 240 MHz and is located at the prime focus of the GBT. The other is the L-band receiver, which spans from 1.15 to 1.73 GHz and is installed in the rotating turret at the Gregorian focus of the GBT¹. The reason for using two different receivers is so that the pulsar signal can be measured across a wide range of frequencies. This is necessary because pulsar signals are subject to frequency-dependent dispersion during their journey through the interstellar medium (ISM). Free electrons in the ISM form a plasma, which means the frequency of light that is allowed to propagate through the plasma is limited by the plasma frequency

$$\nu_p = \sqrt{\frac{e^2 n_e}{\pi m_e}} \quad (1.1)$$

¹<https://science.nrao.edu/facilities/gbt/proposing/GBTpg.pdf>

where e is the charge of an electron and m_e is the mass of electron. The plasma frequency is set by the number density of free electrons in the plasma, n_e . Light with a frequency lower than the plasma frequency will not propagate through the plasma (Condon & Ransom 2016). This hard cutoff is due to the index of refraction for the plasma

$$\mu = \sqrt{1 - \left(\frac{\nu_p}{\nu}\right)^2} \quad (1.2)$$

where ν is the frequency of the light. When ν is less than ν_p , the index of refraction becomes imaginary, which means that the plasma is opaque to that frequency (Condon & Ransom 2016). The propagation speed of the light changes due to the non-vacuum index of refraction. The group velocity, v_g , of the light is the product of the index of refraction and the vacuum speed of light.

$$v_g = c\sqrt{1 - \left(\frac{\nu_p}{\nu}\right)^2} \quad (1.3)$$

Thus, the speed at which light moves through the plasma is frequency-dependent. Lower-frequency waves are delayed more than higher-frequency waves. An example of this dispersion is shown in Figure 1.2. We must be able to observe as much of the pulse as possible in frequency space in order to accurately determine its time of arrival.

This dispersion is also time-dependent, so observing a pulsar at vastly different times reduces timing accuracy, with errors on the order of 50 ns for observations separated by 14 days (Lam et al. 2015). Given the distinct locations of the two receivers used by NANOGrav for pulsar timing with the GBT (prime focus and Gregorian focus), observations of a given pulsar are usually separated by several days. For this reason, a large bandwidth is a key design requirement for future pulsar timing experiments so that only one receiver needs to be used.

A new radio receiver for NANOGrav is being developed at Green Bank Observatory for the GBT. The design for this receiver closely resembles the receiver that has recently been developed for the Parkes radio telescope (Dunning et al. 2015). Because the receiver's design specifications are optimized for pulsar observations, its commissioning will ensure the GBT's status as a premier telescope for pulsar

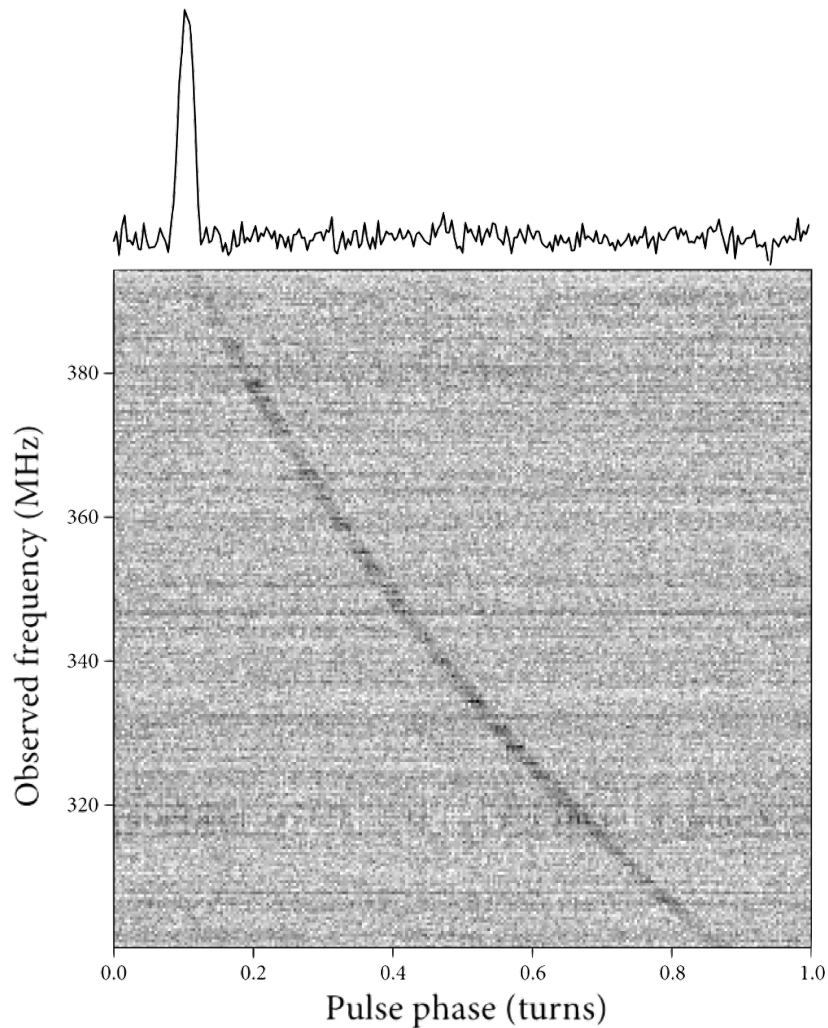


FIGURE 1.2: An observation of a pulsar pulse being spread out in frequency over time. The de-dispersed pulse is shown above the plot. The first frequency detected in this plot is higher than all later frequencies detected, indicating that higher-frequency components of the signal move through the ISM faster than lower-frequency components. Adapted from [Condon & Ransom \(2016\)](#).

timing. The new ultra-wideband (UWB) receiver for the GBT is sensitive to radiation at frequencies ranging from 700 MHz to 4.2 GHz. This is a bandwidth of 3.5 GHz, over four times the combined bandwidths of the 800 MHz and L-band receivers.

CHAPTER 2: Background

2.1 Pulsars

When a supergiant star reaches the end of its life cycle, its fusion processes cease and the iron core of the star collapses under gravity due to a loss of hydrostatic equilibrium (Carroll & Ostlie 2017). This collapse causes the bulk of the stellar material to ricochet off of the core and the star ends its life in a supernova explosion, where the star throws off its lighter outer layers and the stellar core is all that remains at the original location of the star. Because of the large inward forces during the collapse, the atoms in the core undergo neutronization, in which a large neutron-rich nucleus is formed due to electron capture by protons (Carroll & Ostlie 2017). So, the remnant core is called a neutron star. A typical neutron star contains between 1.4 and 2 solar masses of neutrons and ions on average, but is only tens of kilometers in diameter (Condon & Ransom 2016; Lorimer & Kramer 2005). Due to the conservation of angular momentum and magnetic flux during their progenitor's collapse, pulsars rotate extremely fast—up to 700 rotations per second—and have strong magnetic fields up to 10^{14} gauss (Condon & Ransom 2016). Little is known about the state of neutron star interiors (Condon & Ransom 2016; Lorimer & Kramer 2005), but the environment is no doubt extreme and likely contributes to the observational properties of neutron stars. A pulsar is a neutron star that we can see pulsed radiation from due to the neutron star's periodic rotation.

The mechanisms by which pulsars radiate are not well-understood (Lorimer & Kramer 2005), although there are many theories about emission mechanisms in the radio portion of the electromagnetic spectrum as well as at higher energies. A depiction of a pulsar is shown in Figure 2.1. Pulsars are thought to radiate due to charged particles in the star's atmosphere accelerating along open magnetic field lines that reach far from the pulsar (Carroll & Ostlie 2017). Because of the paths of the charged particles, the pulsar emits beams of radio waves along its magnetic axes, the directions at which the magnetic field points directly towards and away

from the pulsar. As the pulsar rotates, the beams of radiation extending from its magnetic axes sweep through space, and if one happens to strike the Earth, we see a pulse.

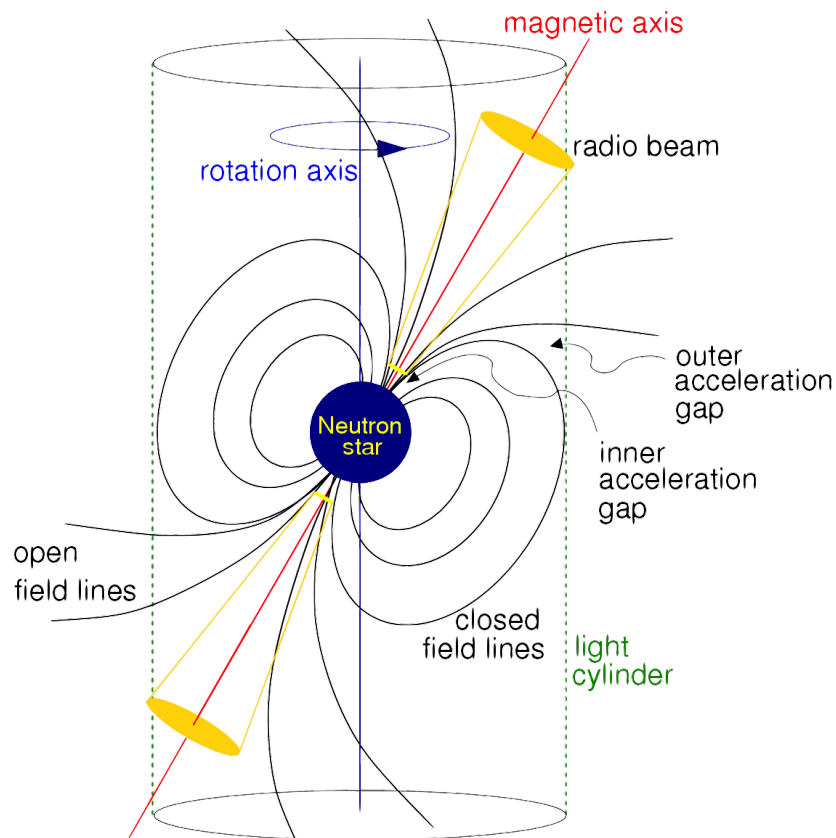


FIGURE 2.1: A cartoon depiction of a pulsar. An offset between the magnetic axis and rotation axis allows the pulsar's radio beams to sweep through space and occasionally intersect with Earth, allowing the pulsar to be observed.

Adapted from [Lorimer & Kramer \(2005\)](#).

Pulsars have a natural tendency to slow their rotation over time. A typical pulsar spin-down rate is about 10^{-15} , and is measured in seconds of period change per second ([Carroll & Ostlie 2017](#)). However, the faster a pulsar rotates, the more stable its rotational period with time. Pulsars that have rotation periods on the order of milliseconds have a large rotational kinetic energy because of their high spin rate ([Lorimer & Kramer 2005](#)). They also tend to have lower spin-down rates due to their high rotational moment of inertia. These characteristics make millisecond pulsars very good clocks: we can be reasonably sure that their pulses will reach us at a regular cadence.

2.2 Pulsar Timing

Beyond pulsar spin-down, other effects can change the observed period of a pulsar. For instance, “glitches” in the pulsar’s pulse period can occur due to physical changes in the pulsar. For instance, while the pulsar ages and experiences spin-down, the outer layers of the pulsar may readjust themselves to compensate for the reduced rotational kinetic energy (Carroll & Ostlie 2017). This effectively decreases the radius of the pulsar, which in turn increases its rotation speed, conserving angular momentum. We would observe this as a decrease in the pulsar’s rotation period.

A pulsar’s spin-down rate as well as its glitches are unique from pulsar to pulsar. Though glitches are unpredictable, spin-down rate can be measured through observations. So, if we account for spin-down and the potential for glitches, any unexplained variations in the observed period of a pulsar should be caused by something external to the pulsar. Pulsars can be used to detect gravitational waves, or propagating disturbances in space and time.

We can measure pulsar signal times-of-arrival (TOAs) using radio telescopes. When we have a set of measured TOAs for a given pulsar, we can subtract a predicted set of TOAs from them to account for the pulsar’s measured spin-down rate among many other corrections. Then, we are left with timing residuals. If we observe many pulsars over a period of many years, we may be able to detect correlation between timing residuals of different pulsars. The fact that these residuals are correlated between multiple pulsars suggests that they could be caused by a gravitational wave passing through the space between the Earth and the pulsars. This means that the apparent pulse periods have changed due to the expansion and contraction of that space.

Changes in timing residuals due to a gravitational wave are predicted to be extremely small, and thus require that pulsars be timed with high accuracy. This is the goal of the North American Nanohertz Observatory for Gravitational Waves (NANOGrav). They observe a subsection of pulsars in the International Pulsar

Timing Array (IPTA)¹. The IPTA is a consortium of three other entities (the European Pulsar Timing Array, NANOGrav, and the Parkes Pulsar Timing Array) that together observe around 100 millisecond pulsars, which are pulsars with the smallest pulse period known and therefore the most stable timing.

Gravitational waves are predicted to have particular signals in the timing residuals of an array of pulsars. To be specific, the correlation in residuals will be high for pulsars close in angular distance on the sky, and pulsars that are separated by a large angular distance will have timing residuals that are either uncorrelated or negatively correlated (Condon & Ransom 2016; NANOGrav Collaboration et al. 2015). In addition to spatial correlation, temporal correlation in timing residuals will be produced by gravitation waves due to the fact that they oscillate in time.

2.3 Waveguides

Before discussing the characteristics of the UWB receiver, it is pertinent to discuss properties of radio receivers as a group. A receiver (sometimes called a feed horn or even an antenna) is essentially a highly specialized waveguide. Waveguides are conductors that can transmit radio frequency light from one location to another. They typically take the form of hollow metal pipes with circular or rectangular cross-sections. These metal waveguides are commonly used at microwave frequencies of around 3 GHz to 300 GHz (Carroll & Ostlie 2017), taking over for conventional cables which stop successfully transmitting light at around 500 MHz (Laverghetta 1976). Optical fibers are another form of waveguide which can be used to transmit light in the optical region of the electromagnetic spectrum, although they are not governed by identical physics to waveguides. Waveguides “guide waves” by enforcing boundary conditions on their inner conducting surfaces. In addition to keeping the waves confined within the walls of the waveguide, these conditions along with the waveguide dimensions place restrictions on the frequencies of waves which are allowed to propagate through a waveguide.

A complete discussion of the theory behind waveguide modes is beyond the scope of this thesis. However, some qualitative analysis will build the background necessary

¹<http://www.ipta4gw.org/>

for understanding how light propagates in radio receivers. A rectangular waveguide is a useful example for visualizing how waves propagate down a waveguide. A depiction of a rectangular waveguide is shown in Figure 2.2. We can imagine light as a propagating wave with two perpendicular components, E and B . There are two types of light that can propagate down this waveguide: transverse electric (TE) and transverse magnetic (TM) waves. TE waves are characterized by their electric field component E having no oscillation in the longitudinal direction of the waveguide (Griffiths 2013). This direction is z in Figure 2.2. TM waves have no magnetic field component oscillation down the longitudinal axis. The boundary conditions in a waveguide allow light to propagate in quantized modes down the waveguide. These modes are denoted by the indices m and n , where m typically corresponds with the larger cross-sectional dimension of the waveguide (Griffiths 2013).

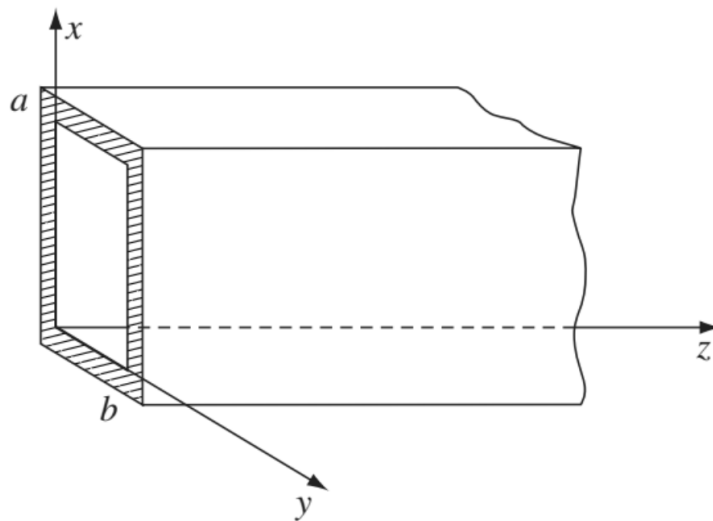


FIGURE 2.2: A depiction of a rectangular waveguide. The frequencies of light allowed to propagate in the waveguide are related to its dimensions a and b . Adapted from Griffiths (2013).

Waveguides are perfect high-pass filters. For a given waveguide with a certain geometry, there exists a frequency below which radiation cannot propagate down the waveguide in each waveguide mode. This is called the cutoff frequency of the mode, the expression for which is given by

$$\omega_{mn} = c\pi\sqrt{(m/a)^2 + (n/b)^2} \quad (2.1)$$

where c is the speed of light and a and b are the waveguide dimensions (Griffiths 2013). The feed horn on a radio receiver can be thought of as a waveguide with a varying diameter (Beukman et al. 2016). Feed horns are used to collect radiation into a small cross-sectional area to be collected. Their varying diameter introduces some complications when calculating the cutoff frequencies for the horn, as they would vary with the changing diameter. This difficulty is a motivation for using software to model the frequency response of receivers.

2.4 Radio Receivers

A straightforward way to characterize a receiver is by its gain, or how good it is at receiving radiation from different angles. The gain of an antenna as a function of solid angle on the sky is often called the far-field radiation pattern of the antenna. The far-field pattern of a receiver is used in calculating the receiver's efficiency. Different far-field patterns are desirable for different antennas, but since many radio telescopes with large reflector dishes are structurally similar, the desired far-field pattern for a radio receiver for astronomy tends to adopt one of a few basic profiles. An example of a far-field pattern is shown in Figure 2.3. Note its high sensitivity in one direction with decreased sensitivity at the side lobes and back lobe.

In radio astronomy, antennas are used to receive radiation from distant sources. Antennas are used in many applications besides radio astronomy, often in both transmitting and receiving modes. An antenna can be characterized based on either its transmitting or receiving properties without loss of information. This is due to the principle of electromagnetic reciprocity. We can approach the concept of electromagnetic reciprocity from two different angles. The first appeals to logic: it is easier to calculate the transmitting gain of an antenna than its collecting area. We cannot generate perfect point sources in simulation software due to the discretized nature of numerical simulations. The second angle appeals to the time symmetry of the equations which govern the radiation patterns of an antenna. Any solution to Maxwell's equations for electric and magnetic fields are symmetric when time is reversed ($\vec{E}(r, t) \equiv \vec{E}(r, -t)$). Therefore, it is mathematically

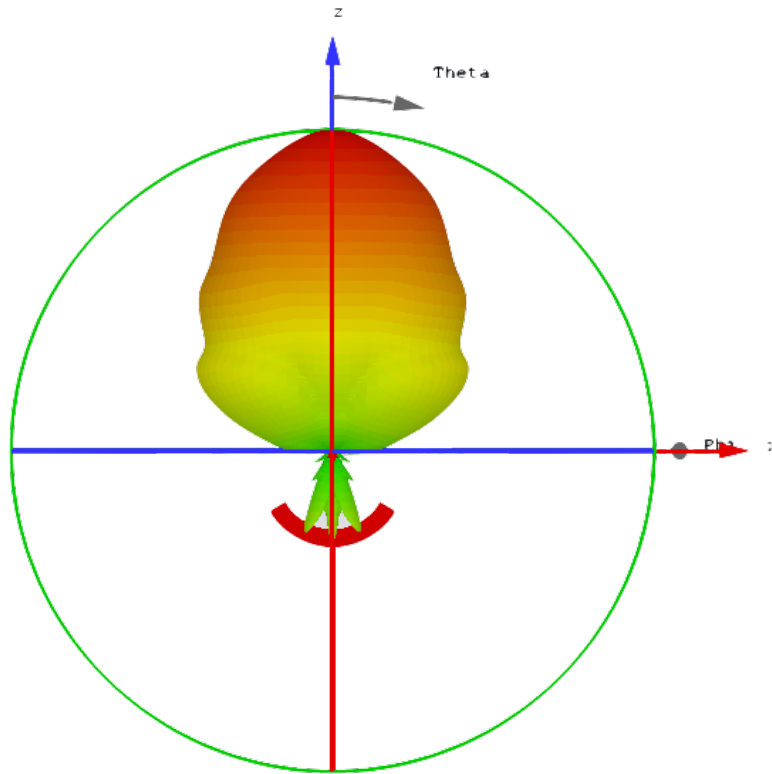


FIGURE 2.3: A model of the three-dimensional far-field pattern for the UWB receiver at 4.2 GHz. It exhibits a high gain in the forward direction and lower gain at the side lobes and back lobe, typical of a radio receiver for installation on a telescope like the GBT.

valid to consider a transmitting antenna as a receiving antenna and visa-versa as there is no practical difference between the two (Johnson 1993). Sometimes, it is more convenient to take one perspective than another in order to make conceptualizations and calculations easier, but the results have the same meaning no matter the intended purpose of the antenna.

CHAPTER 3: UWB Receiver Efficiency

3.1 Receiver Specifications and Models

Steve White, an engineer at Green Bank Observatory, has been working on the design of the UWB receiver for the past two years. The design of the receiver has been primarily performed in CST Microwave Studio, with some additional analysis performed in Microwave Office. The current design of the feed horn of the receiver is shown in Figure 3.1 in a perspective view and in Figure 3.2 in a side view.

The design of the UWB receiver has a few distinct features that extend the bandwidth of the horn. The first features are ridges on the inside of the horn that lead into the throat. These lower the cutoff frequency of the dominant mode in the horn by up to a factor of four (Akiray 2013). Therefore, their presence extends the bandwidth of the receiver to lower frequencies. The UWB receiver is quad-ridged, which means there are four ridges with identical profiles equally spaced around the interior of the horn. Also, for the upper end of the bandwidth, a dielectric spear placed in the center of the horn reduces detrimental beam properties that arise at high frequencies (Dunning et al. 2015). The spear has a quartz center which is surrounded by two matching layers both made of Teflon. The inner Teflon layer is solid Teflon, and the outer Teflon layer has cut-out grooves, making it approximate a material with a dielectric constant between that of Teflon and a vacuum. The matching layers provide impedance matching between the quartz and the vacuum inside the horn.

3.1.1 Receiver Models

The design of the UWB receiver has been an iterative process permitted by the use of design software. Because of this iterative process, an explanation of model milestones is required to fully understand the results presented in this thesis. We divide our design process into four distinct models which are identified by unique characteristics. These models are summarized in Table 3.1. The first model, Model

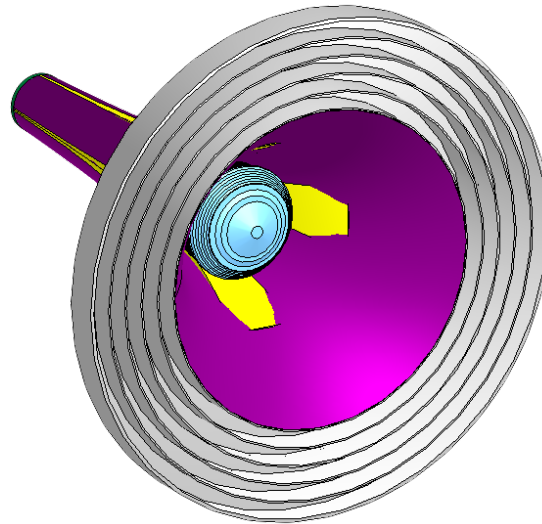


FIGURE 3.1: A perspective view of the UWB receiver feed horn. The corrugated skirt encircles the aperture. Two of the ridges are visible along the walls of the receiver. The outer matching layers on the dielectric spear are also visible in the center of the throat.

A, was finalized during the summer of 2019. It included the corrugated skirt and a dielectric spear, but did not include Teflon matching layers around the quartz spear. It also included a vital component of the cryogenic system, the waveguide window, at the aperture of the receiver (see Section 4.1 for a description of the window).

A large thermal gap in the receiver body between the window and the dielectric spear was required in order to isolate the cryogenically-cooled dielectric spear from the window, which touches the outside world. This gap was not included in Model A. When the thermal gap was added to the model, it caused the radiation pattern to deviate from the ideal shape due to its size, which prompted us to design a smaller and thinner window inset into the throat of the receiver in further iterations. Models B, C, and D include this smaller window. Model B will be used as a model for comparison, as it does not include the dielectric spear or the Teflon matching layers around it. Model C includes the spear but not the matching layers. Model D is the most complete model, including both the spear and matching layers.

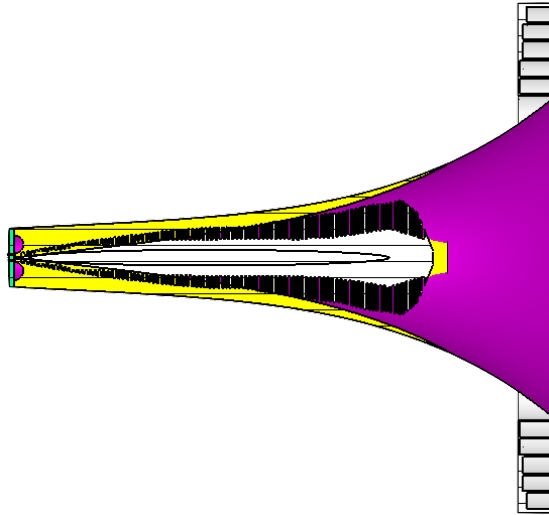


FIGURE 3.2: A side view of the UWB receiver feed horn. The receiver is cut in half in this visualization in order to see the inside in more detail. The corrugated skirt is visible at the edge of the aperture. The flared body of the feed horn is apparent. The ridge profiles are also shown. The dielectric spear (ovoid shape) and its outer matching layers are shown in detail.

Model name	Window	Spear	Teflon	Thermal gap	Identifying factor
Model A	Large	Yes	No	No	Large window
Model B	Small	No	No	Yes	No dielectric
Model C	Small	Yes	No	Yes	No teflon layers
Model D	Small	Yes	Yes	Yes	Teflon layers

TABLE 3.1: Iterations of UWB receiver models. Model A features a large waveguide window which consequently produces poor radiation patterns when the required thermal gap was added to the model. Models B, C, and D feature a smaller window and various combinations of other required components to show the effects of including those components in the model.

3.2 Receiver Efficiency

The feed efficiency (e_{tot}) of an antenna is the proportion of the radiation that is collected by the reflector dish which actually gets received and recorded by the feed. An antenna's feed efficiency depends on the shape of its radiation pattern. Because the radiation pattern of an antenna depends on the receiving frequency, the feed efficiency is also frequency-dependent. It is important to characterize the efficiency of an antenna during the design phase in order to know that the receiver

will be integrable with the telescope. The design goal for the UWB receiver was to achieve a feed efficiency between 60% and 70% at the lower end of the frequency range and above 50% at higher frequencies.

It has been established by Ludwig (1965), Collin (1984), and Kildal (1985) that the feed efficiency can be divided into several sub-efficiencies that, when multiplied, contribute to the total feed efficiency. These sub-efficiencies include those due to spillover radiation from the ground or the sky over the edge of the dish (e_{sp}), inefficient illumination of the dish (e_{ill}), phase errors at the aperture (e_{ph}), and losses due to cross-polarization (e_{xp}). Other causes of reduced efficiency include loss of signal due to obstructions to the aperture of the telescope, like struts that hold receivers above main reflectors. There is also additional spillover of radiation that can come from a subreflector if a telescope has a Cassegrain or Gregorian focus. However, the GBT's prime focus receivers are exempt from these sub-efficiencies, as the aperture of the GBT at prime focus is unblocked because of its offset design (Norrod & Srikanth 1996). Our goal was to maximize the product of each of these sub-efficiencies:

$$e_{tot} = e_{sp} \cdot e_{ill} \cdot e_{ph} \cdot e_{xp} \quad (3.1)$$

A more detailed discussion of each sub-efficiency follows.

3.2.1 Spillover Efficiency

Spillover is more easily understood if we consider the feed horn as a transmitter. As its name implies, spillover is radiation that “spills over” the edge of the dish after being emitted by the feed horn and hits the ground instead of the reflector. Conversely, when considering the feed horn as a receiver, spillover is radiation that is accepted by the feed horn from beyond the edge of the dish. See Figure 3.3 for a simplified diagram of where spillover comes from. To calculate the spillover efficiency, or the fraction of radiation emitted by the feed that is not lost to spillover, it is easier to consider the feed horn as a transmitter.

We calculate the spillover efficiency as it is described in Kildal (1985). Because of the geometry of radio telescopes, we know that the radiation that will strike

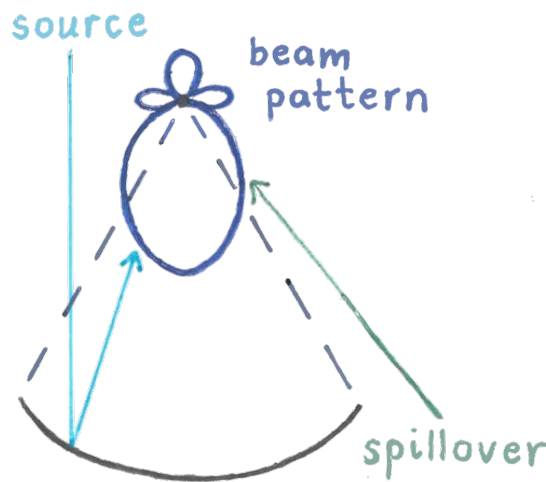


FIGURE 3.3: A simplified schematic of how spillover reaches a receiver. The desirable behavior of a telescope is for radiation from an astronomical source to strike the reflector and reach the beam pattern. However, the beam pattern has sensitivity at angles past the reflector dish, so spillover from past the dish can still be received.

the reflector must be within some angle from the boresight, which points down the center of the feed. For the GBT's prime focus feeds, this half-angle is about 39° from the boresight. This is determined purely geometrically and describes the angular distance from the center of the dish to the edge measured as if one was floating at the focal point of the telescope.

When we integrate in a line along the dish (along θ), we capture a slice of the radiation pattern. We then divide this by the same integral with limits from the boresight to 180° , which captures all of the radiation emitted by the main lobe of the receiver in our slice. In equation form, the spillover efficiency is

$$e_{sp} = \frac{\int_0^{\theta_0} [|CO(\theta)|^2 + |XP(\theta)|^2] \sin(\theta) d\theta}{\int_0^\pi [|CO(\theta)|^2 + |XP(\theta)|^2] \sin(\theta) d\theta} \quad (3.2)$$

As we can see, the numerator involves an integration across the dish and the denominator involves an integration from 0 to 180° . The exact expression inside the integral in both cases measures the power in the co-polar and cross-polar radiation patterns, $CO(\theta)$ and $XP(\theta)$ respectively.

Both the co-polar and cross-polar radiation patterns represent the gain as a function of θ for different testing environments. Ludwig (1973) describes the preferred definition of “cross-polarization” as follows. In software, the gain of a receiver is calculated by measuring its sensitivity to radiation from another transmitter. The co-polar radiation pattern is measured when the polarization of the receiver and transmitter are the same, and the cross-polar radiation pattern is measured when the polarization of the receiver is orthogonal to the polarization of the transmitter. For circularly polarized light, the receiver would be sensitive to, for example, right-handed circular polarization, while the transmitter would be emitting left-handed circular polarization. For linear polarization, the transmitter would be emitting light whose E -field oscillation is 90° separated from the light that the receiver is sensitive to.

3.2.2 Illumination Efficiency

The concept of illumination efficiency is rather simple and is easier to conceptualize when considering a transmitting antenna. It is a measure of how much the actual radiation pattern of an antenna deviates from a uniform function across the aperture which drops to zero outside of the reflector (described by the half-angle subtended by the reflector; 39° from the boresight for the GBT). Our goal radiation pattern is not a uniform response across the aperture, as it is impossible to perfectly square-off the edge of the beam pattern at the edge of the reflector at all frequencies simultaneously and we would like to avoid spillover. We instead use a Gaussian beam shape which tapers towards zero at the edges. It has been determined that a -17 dB taper at the edges of the reflector is the most optimum taper (Steve White, personal correspondence). The expression that we used to calculate the illumination efficiency can be found in Kildal (1985).

The relationship between spillover and illumination is the most important relationship to balance when designing an antenna because they are most closely related to the shape of the beam. A receiver that has excellent spillover efficiency might have poor illumination efficiency because it is not utilizing the reflector’s area well. Similarly, a receiver that has a very high illumination efficiency is more likely to suffer from inefficiency due to signal loss over the sides of the dish.

3.2.3 Cross-polarization and Phase Efficiencies

The final two sub-efficiencies that we consider are more mathematically and conceptually complicated than spillover and illumination. A detailed discussion of their origin is beyond the scope of this thesis. The equations for calculating cross-polarization and phase efficiency can be found in [Kildal \(1985\)](#). They are caused by fields interacting destructively in the aperture of the telescope. Cross-polarization losses are due to signal being transferred from one polarization to the orthogonal one. Phase losses happen due to geometric imperfections in the reflector dish causing different modal components of the light to be out of phase with each other in the aperture.

3.3 Efficiency Analysis

Each of the sub-efficiencies mentioned above were calculated given the simulated far-field patterns for the various models of the UWB receiver. We calculated the far-field patterns as a function of receiving frequency in 100 MHz steps between 700 MHz and 4.2 GHz. In order to summarize the shape of the three-dimensional radiation pattern at each frequency, we took three two-dimensional “cuts” through the far-field pattern as a function of the azimuthal angle about the axis of symmetry of the feed horn. These cuts are at 0° , 45° , and 90° , and are called the E, D, and H planes respectively. The angles are defined in reference to the polarization angle of the radiation used in the simulation. A visualization of the cuts is shown in [Figure 3.4](#).

We only calculate the cross-polarization efficiency for the 45° cut across the far-field pattern, as it represents the angle at which there is the most cross-polarization and thus where the efficiency is the worst. [Kildal \(1985\)](#) explains that it is unphysical to use the equation presented to determine the cross-polarization efficiency for the 0° and 90° cuts. To ensure cross-polarization was not high at these cuts, we observed the simulated far-field pattern for the 0° and 90° cuts and verified that the cross-polarized field is 20 dB down from the co-polarized field.

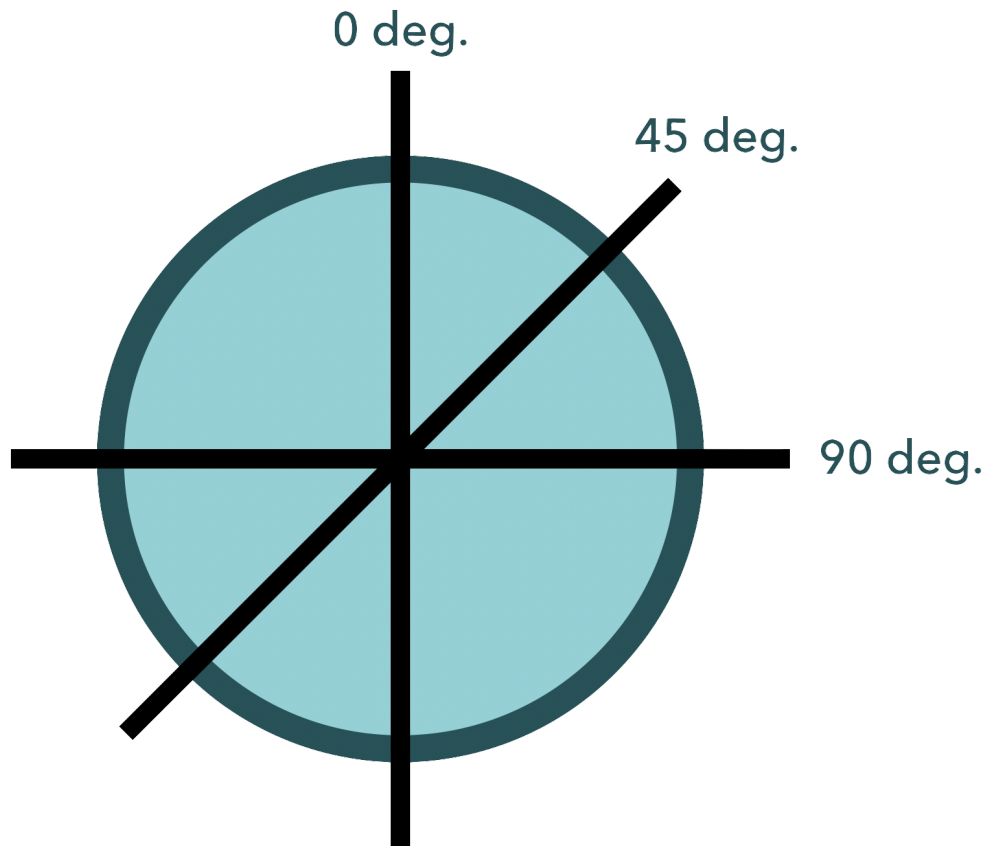


FIGURE 3.4: A diagram illustrating the two-dimensional cuts through the three-dimensional radiation pattern. In the diagram, the viewer is looking at the receiver face-on, and the teal circle represents the outer edge of the receiver.

The equations for each of the sub-efficiencies were written in MATLAB by a previous GBO summer student, Ellen Robertson. This analysis of the sub-efficiencies of a receiver design is the most detailed one that GBO has performed; in the past only the total efficiency was calculated and there was no detailed look at the individual causes of reduced performance. For Model A (with the large window and no matching layers), the UWB receiver's predicted feed efficiency (solid line) and sub-efficiencies as a function of frequency are shown in Figures 3.5, 3.6, and 3.7 for the 0° , 45° , and 90° cuts respectively. The design goals of around 60% to 70% efficiency at lower frequencies and above 50% efficiency at higher frequencies are quite close to being met, save for a large drop in efficiency at 2.9 GHz for the H plane cut through the far-field pattern. A potential method for mitigation of this drop will be discussed in Section 5.1, although we do not anticipate that it will significantly affect the performance of the receiver.

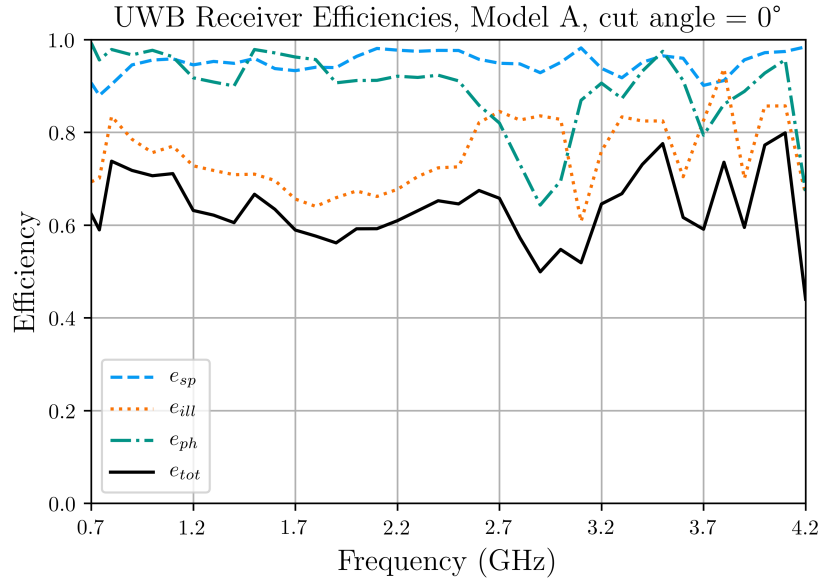


FIGURE 3.5: The total efficiency (solid line) and sub-efficiencies (non-solid lines) for Model A of the UWB receiver across its entire bandwidth for a 0° cut across the far-field pattern (E plane). Note that the total efficiency is around 60% for the lower half of the bandwidth and still above 50% for the higher half of the bandwidth.

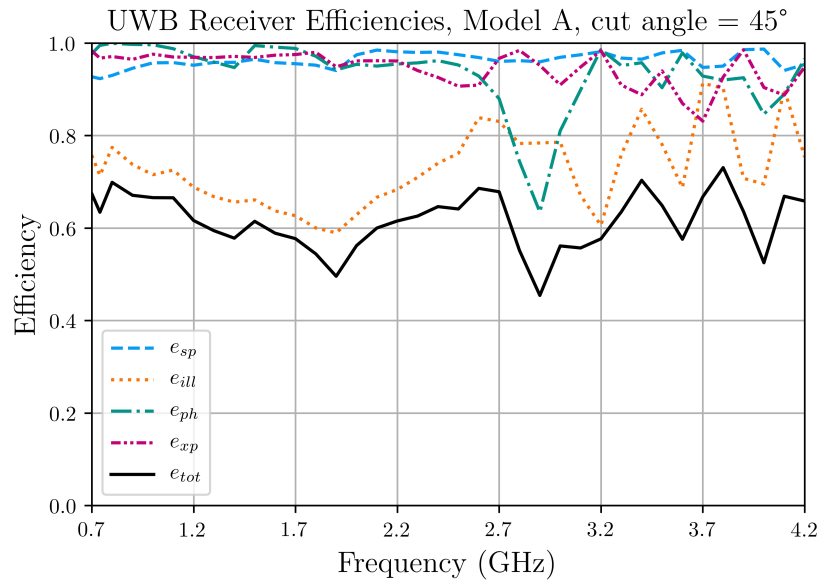


FIGURE 3.6: The total efficiency (solid line) and sub-efficiencies (non-solid lines) for Model A of the UWB receiver across its entire bandwidth for a 45° cut across the far-field pattern (D plane). The design goals are still quite close to being met, although the efficiency drops below 60% for lower frequencies. A dip in total efficiency at 2.9 GHz is slightly more visible in the 45° cut than in the 0° cut.

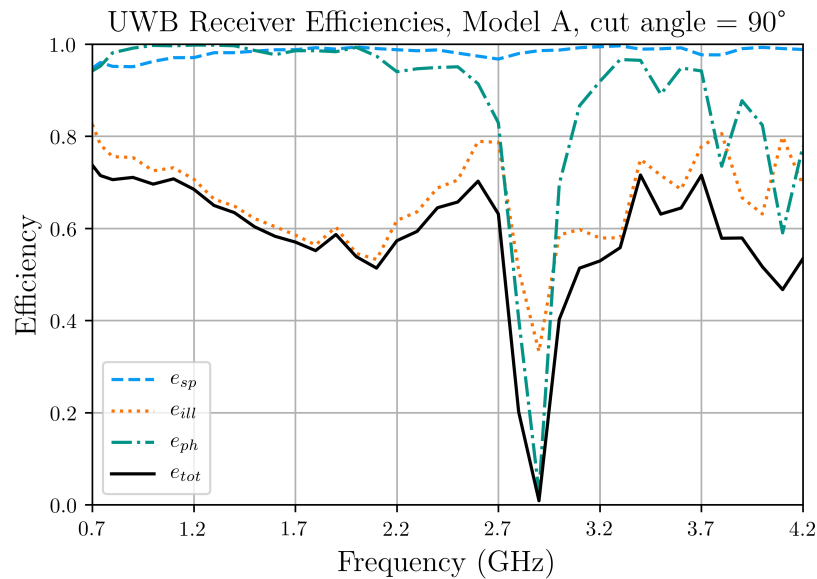


FIGURE 3.7: The total efficiency (solid line) and sub-efficiencies (non-solid lines) for Model A of the UWB receiver across its entire bandwidth for a 90° cut across the far-field pattern (H plane). A significant dip in phase efficiency causes reduced performance at 2.9 GHz.

After making the window smaller, we considered Model B, which has no dielectric spear or Teflon matching layers. Dunning et al. (2015) states that a dielectric insert will increase the feed efficiency at higher frequencies. Our model shows this, as removing the dielectric decreases the total efficiency at higher frequencies. Further, we can also conclude that this is mainly due to decreased phase and illumination efficiencies.

When we include the spear but no matching layers in Model C, we can see that the baseline level of the efficiencies increases at higher frequencies. However, we still observe a detriment at around 2.9 GHz, especially in the H-plane.

When we include the matching layers in Model D, we notice that the detriment at 2.9 GHz has disappeared. There still appears to be a baseline decrease in total efficiency as we approach higher frequencies, but this can likely be improved by optimizing the design of the Teflon matching layers.

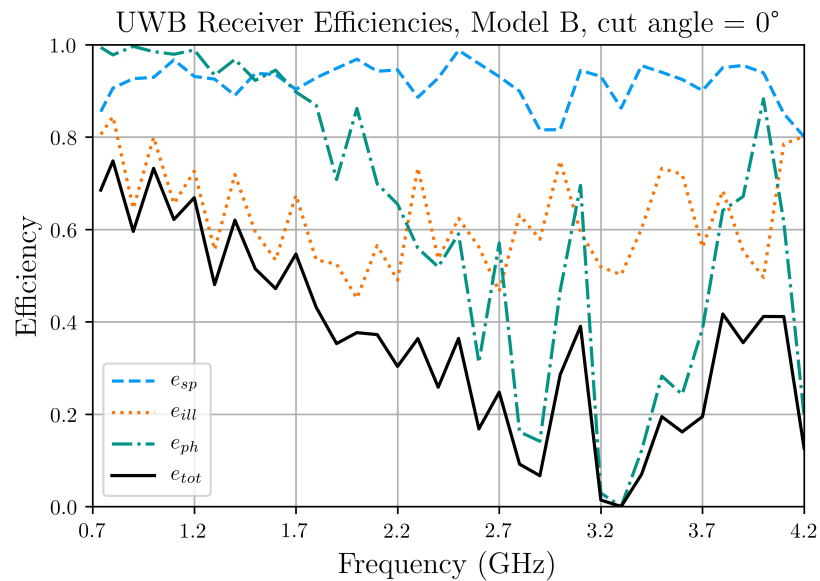


FIGURE 3.8: The total efficiency (solid line) and sub-efficiencies (non-solid lines) for Model B of the UWB receiver across its entire bandwidth for a 0° cut across the far-field pattern (E plane). Note the extreme reduction in efficiency above about 2.7 GHz.

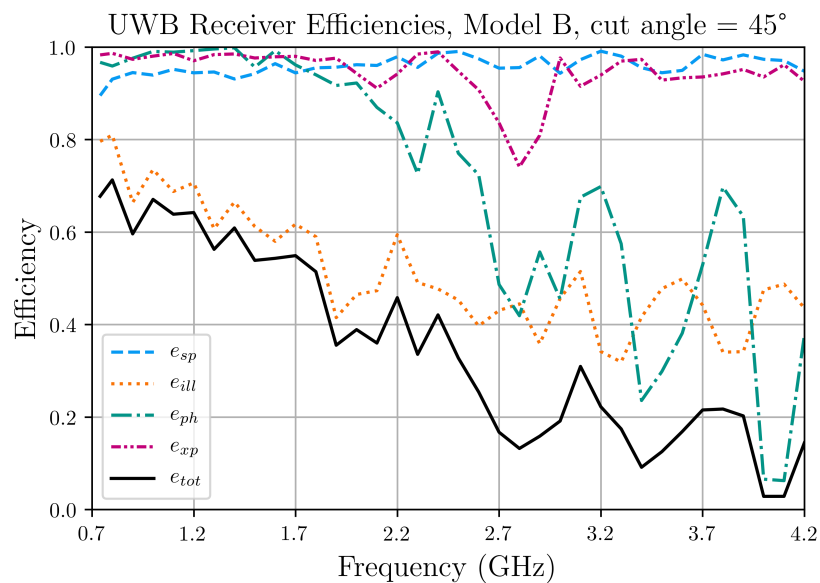


FIGURE 3.9: The total efficiency (solid line) and sub-efficiencies (non-solid lines) for Model B of the UWB receiver across its entire bandwidth for a 45° cut across the far-field pattern (D plane).

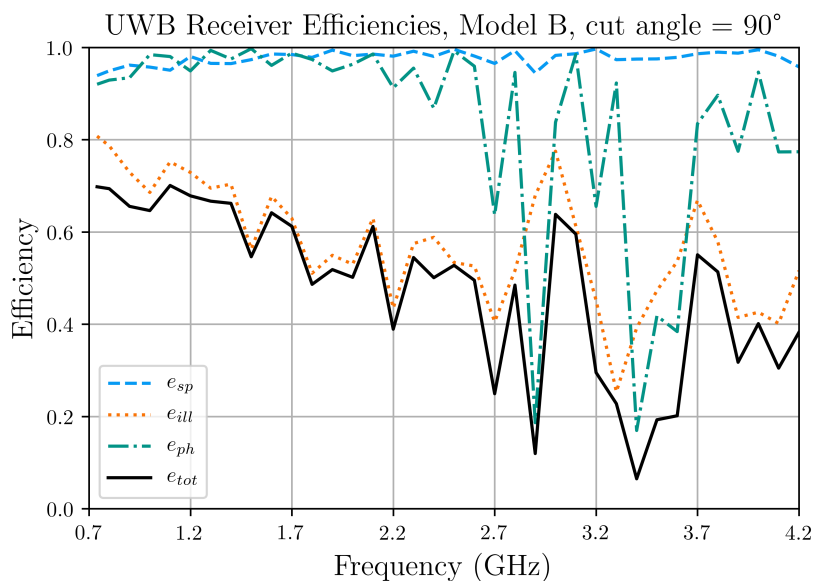


FIGURE 3.10: The total efficiency (solid line) and sub-efficiencies (non-solid lines) for Model B of the UWB receiver across its entire bandwidth for a 90° cut across the far-field pattern (H plane).

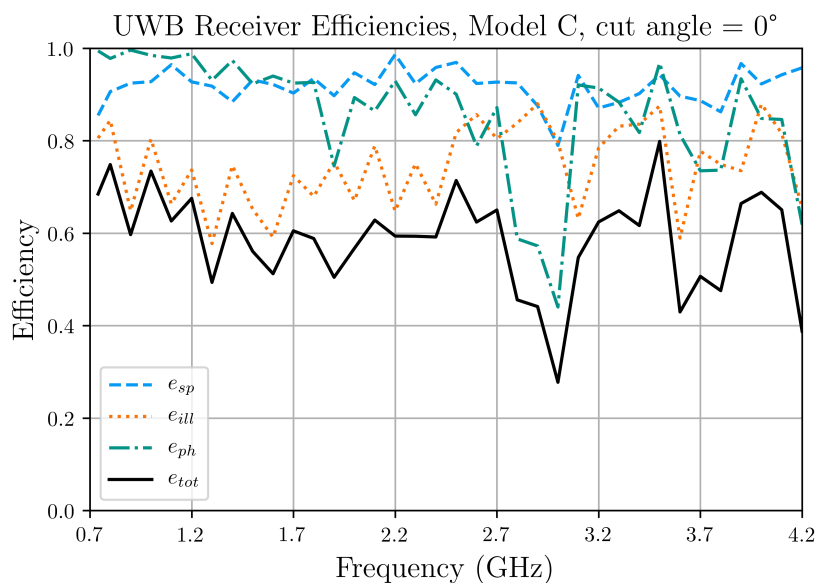


FIGURE 3.11: The total efficiency (solid line) and sub-efficiencies (non-solid lines) for Model C of the UWB receiver across its entire bandwidth for a 0° cut across the far-field pattern (E plane). Note the improved efficiency at high frequencies.

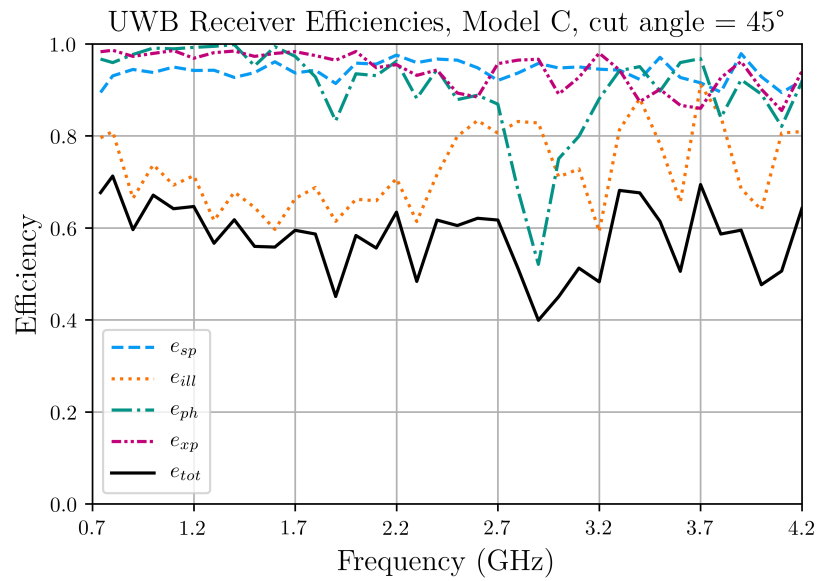


FIGURE 3.12: The total efficiency (solid line) and sub-efficiencies (non-solid lines) for Model C of the UWB receiver across its entire bandwidth for a 45° cut across the far-field pattern (D plane).

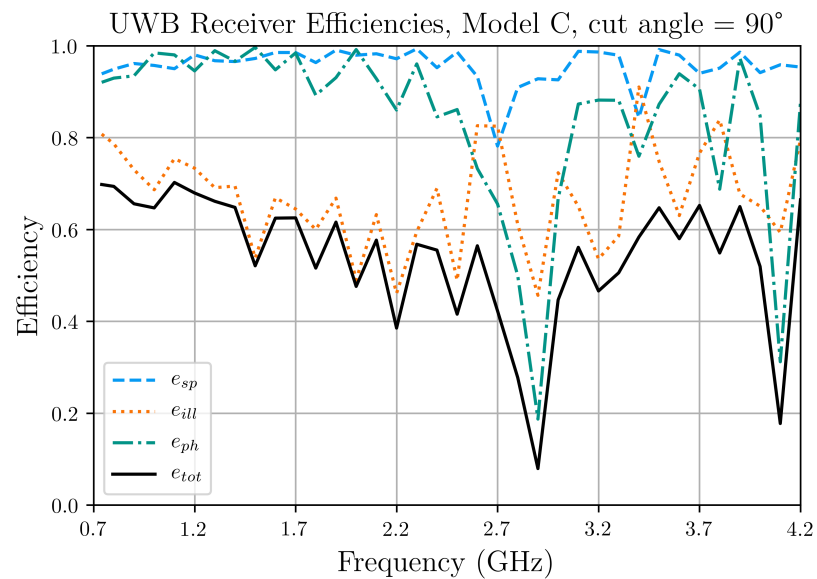


FIGURE 3.13: The total efficiency (solid line) and sub-efficiencies (non-solid lines) for Model C of the UWB receiver across its entire bandwidth for a 90° cut across the far-field pattern (H plane).

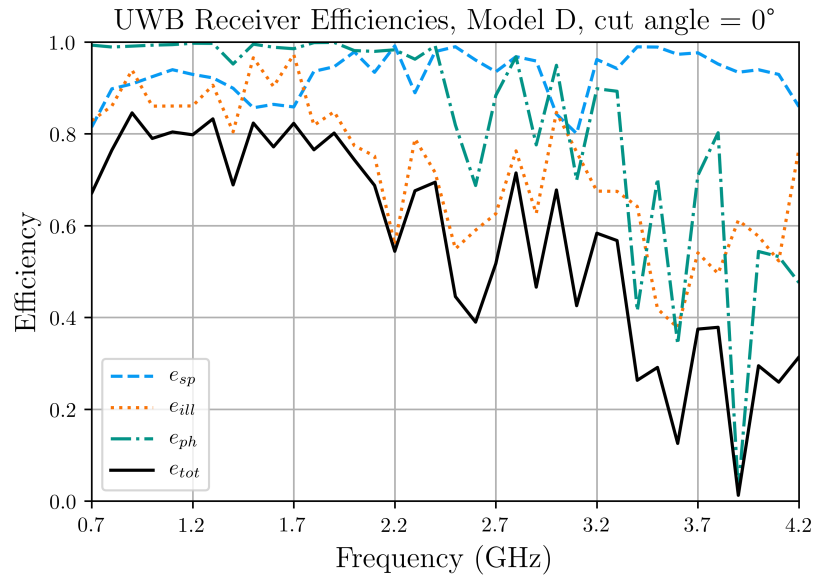


FIGURE 3.14: The total efficiency (solid line) and sub-efficiencies (non-solid lines) for Model D of the UWB receiver across its entire bandwidth for a 0° cut across the far-field pattern (E plane).

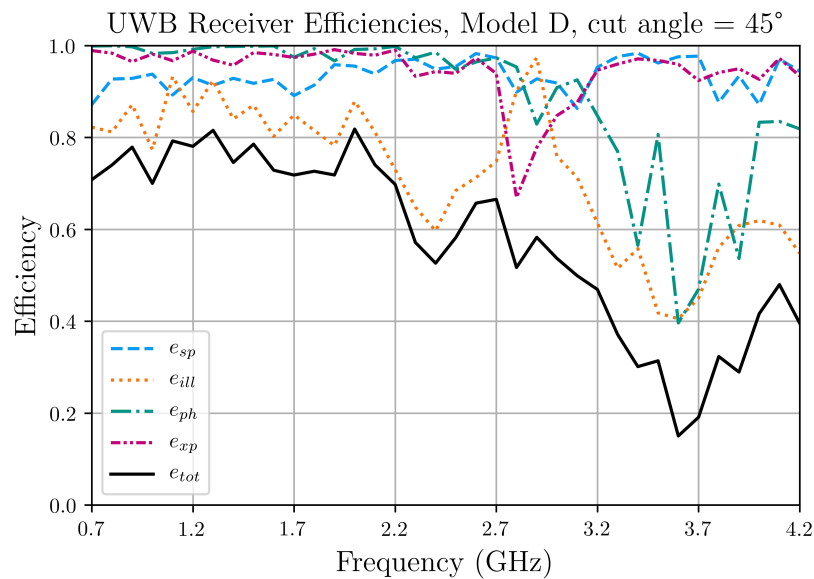


FIGURE 3.15: The total efficiency (solid line) and sub-efficiencies (non-solid lines) for Model D of the UWB receiver across its entire bandwidth for a 45° cut across the far-field pattern (D plane).

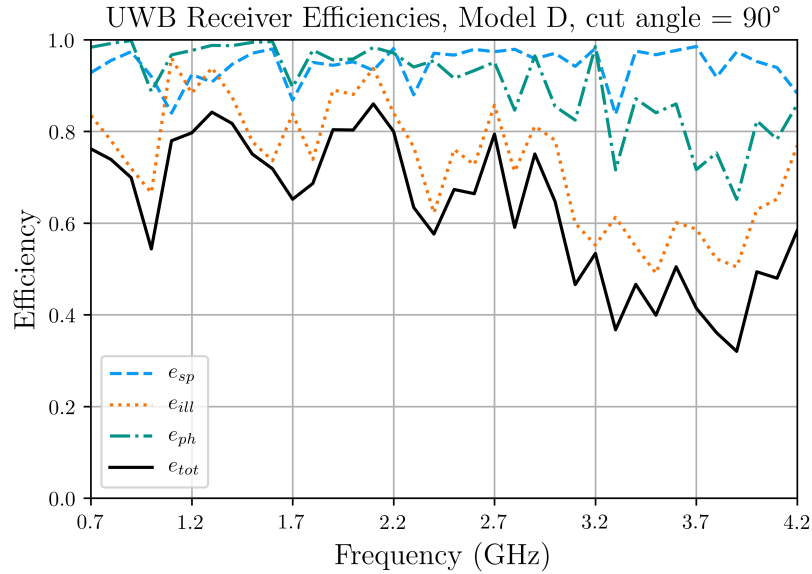


FIGURE 3.16: The total efficiency (solid line) and sub-efficiencies (non-solid lines) for Model D of the UWB receiver across its entire bandwidth for a 90° cut across the far-field pattern (H plane). Note the lack of a significant efficiency detriment at 2.9 GHz.

3.3.1 Spillover Temperature Correction

The spillover temperature is the contribution to the total noise temperature of a telescope that comes from excess radiation “spilling over” from outside the edges of the dish into the receiver. In our calculations, we are actually overestimating the spillover temperature. We attempt to determine the amount by which we are overestimating.

e_{sp} is the fraction of radiation emitted by the receiver that intersects the main reflector of the GBT. Consequently, $1 - e_{sp}$ is the fraction of emitted radiation that does not strike the reflector, also called the relative spillover power. The spillover temperature is traditionally calculated as follows.

$$T_{sp} = (1 - e_{sp}) \cdot T_{ground} \quad (3.3)$$

Here, T_{ground} is the ground temperature, which we take to be 290 K. This calculation only approximates reality because it assumes that the entire part of the beam pattern that does not strike the dish actually strikes the ground. In fact, some of

the beam pattern strikes the cold sky, which has a temperature on the order of 10 K instead of 290 K. A first-order correction to this issue would be to decrease the spillover power that strikes the ground. The back lobe of the radiation pattern would be the primary location for this extra spillover, as it represents a large portion of the radiation pattern. We define the back lobe as the back one-third of the radiation pattern. We can calculate the spillover power in the back lobe of the radiation pattern by adjusting the limits on the spillover efficiency integral:

$$e_{sp} = \frac{\int_0^{\pi/3} [|CO(\theta)|^2 + |XP(\theta)|^2] \sin(\theta) d\theta}{\int_0^{\pi} [|CO(\theta)|^2 + |XP(\theta)|^2] \sin(\theta) d\theta} \quad (3.4)$$

We can then subtract $e_{sp,b}$ from the relative spillover power, $1 - e_{sp}$, to establish that there is a fraction of the radiation pattern that does not see the ground. This is an overcorrection, as we assume that the entirety of the back lobe has zero spillover power, which is false because there is power in the back lobe. We would have to add back in some reduced fraction of the back lobe that sees the ground as well as another fraction that sees the sky in order to be more accurate.

Since we are overcorrecting, the spillover temperature reduction that we calculate is the upper limit for the correction. If the reduction is too small, further corrections are not worth pursuing, as they would only decrease the spillover reduction. Indeed, when we calculate the spillover temperature reduction over a frequency range of 700 MHz to 1500 MHz, we get an average reduction of 0.985 K, which is relatively small compared to an average spillover temperature on the order of 15 to 20 K. The takeaway from this lack of spillover temperature reduction when considering the back lobe contribution is that the majority of the spillover temperature comes from the beam pattern immediately outside of the dish, which is usually facing the warmer ground rather than the cooler sky. It is worth noting that the elevation angle of the GBT affects what fraction of the back lobe sees the sky. At an elevation angle of 5° , the lower limit of the telescope, the portion of the back lobe which sees the sky is only 45.8%. This represents the maximum proportion of the back lobe which can see the sky.

3.3.2 Reflector Edge Angles

During the design process of the GBT, the designers made the decision to point the prime focus receivers slightly off-center on the dish. The boresight is along the axis of symmetry, but it is pointed slightly closer to the far edge of the dish than the near edge. This means that as we take different cuts through the radiation pattern, the maximum angle of radiation which strikes the reflector is not always 39.005° as we had assumed previously. Using edge angles provided by Sivasankaran Srikanth from the NRAO Central Development Laboratory in Charlottesville, Virginia, we determined the effect of this difference on the spillover temperature for this receiver. The edge angles as a function of azimuth are shown in Table 3.2.

Cut angle ($^\circ$)	Near angle ($^\circ$)	Far angle ($^\circ$)
0	44.63	33.37
15	44.51	33.58
30	43.95	34.11
45	43.03	34.96
60	41.80	36.08
75	40.38	37.41
90	38.88	38.88

TABLE 3.2: Edge angles of the reflector for the Green Bank Telescope used in our correction to the receiver spillover temperature. For each cut angle through the radiation pattern, the dish subtends some angle from the boresight. The angle to the near and far sides of the dish are provided. For cut angles past 90° , subtract 90° from the cut angle and switch the near and far side angles to get the desired result.

Using a half angle of 39.005° uniformly captures 78.01° centered on the boresight. When considering the adjusted edge angles, the average total subtended angle is 77.97° . For this receiver, the radiation pattern was such that the spillover temperature was lower by about 1 K on average when considering the adjusted edge angles.

CHAPTER 4: UWB Receiver Window

4.1 Waveguide Windows

The UWB receiver will be housed in a metal dewar and cooled with helium to 15 K. A radio-transparent quartz fabric window will be placed on the front of the feed horn to ensure that radiation can still reach the receiver. Because of the high vacuum required to sustain cryogenic temperatures, the window must be strong enough to withstand great forces (Simon 2005); because of the size of the UWB receiver, the vacuum applies about 20,000 pounds of force on the window. Bob Simon, an engineer at Green Bank, is using a vacuum infusion technique to build a novel waveguide window out of layers of fused quartz fabric bonded together with optical epoxy.

A challenging aspect of designing this window is the large diameter of the UWB feed horn. At the aperture, the feed horn is about 0.9 meters in diameter. A typical geometry for a window might be a flat piece of quartz across the feed horn opening. An example of this type of window is shown at the prime focus of the GBT in Figure 4.1. An alternate geometry must be considered for the UWB window in order to withstand the large amount of inward force. Therefore, a curved window is being designed. A model of the receiver with the window is shown in Figure 4.2 in a perspective view and in Figure 4.3 in a side view. The design for the large window is a section of a sphere which is originally 1 meter in diameter. The section has a height of 9 inches. The window is 0.35 inches thick in the center and 0.55 inches thick along the edges to accommodate for the concentrated force on the edges of the window.

Observations of simulated far-field patterns as well as some cursory mode excitation analysis, the process of which is discussed in Section 5.2, suggests that the presence of the window at the aperture of the receiver causes non-desirable mode excitation. This indicates that the window should be moved into the throat of the receiver, closer to the outer layers of Teflon on the dielectric spear. This should reduce the additional mode excitation and allow for a smaller window, which is



FIGURE 4.1: A photo of a receiver at the prime focus of the Green Bank Telescope which has a flat window. The receiver is the cone-shaped component at the lower left of the image. Credit: B. Saxton, NRAO/AUI/NSF.

desirable for the window's structural stability, as a smaller window size leads to less force on the window. A model of the receiver with the smaller window is shown in Figure 4.4.

4.2 Modeling Window Circuit Properties

One of the final steps in modeling the UWB receiver is incorporating the waveguide window into our CST model to measure the expected effect on the circuit characteristics and far-field patterns of the receiver. The metric we used to determine the window's influence on the receiver's circuit properties is called the S_{11} parameter. If we treat the UWB receiver as a transmitter at the end of a circuit and send a signal towards the receiver, there would be some proportion of the

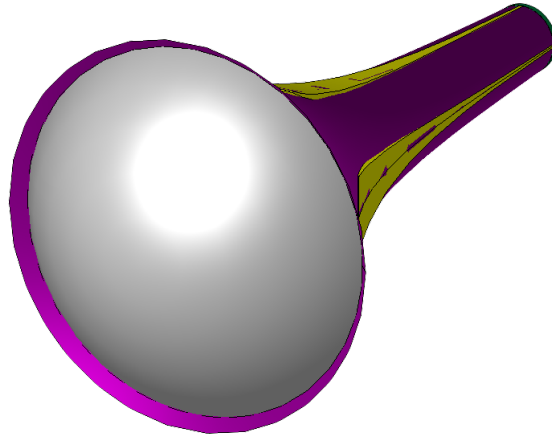


FIGURE 4.2: A perspective view of the UWB receiver feed horn with the window in the aperture included. Note that the corrugated skirt is not included in this diagram. This reflects its removal from the model, where its presence along with the window caused the simulation to run too slowly.

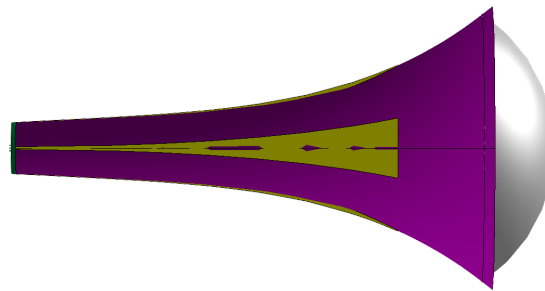


FIGURE 4.3: A side view of the UWB receiver feed horn with the window in the aperture included.

signal that is transmitted by the feed horn and some part that is reflected back due to impedance mismatches. Minimization of this signal reflection when considering a transmitting antenna also improves performance when the antenna is used as a receiver. The S_{11} parameter of a component represents the fractional signal reflected back from that component. The design goal for the S_{11} parameter of the feed horn with a window included is -10 dB or better. If the S_{11} parameter was not better than -10 dB, the input impedance of the receiver would be significantly changed, and it would lose its functionality.

The S_{11} parameters for Model A of the UWB receiver without a window are shown in Figure 4.5. As one might expect, the S_{11} parameter depends on the frequency of the transmitted radiation. The bumps and wiggles in the S_{11} parameter as a function of frequency do not greatly affect the circuit characteristics of the receiver;

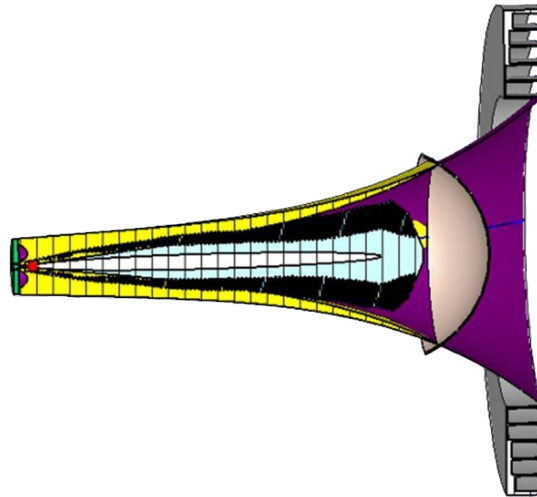


FIGURE 4.4: A side view of the UWB receiver feed horn with a smaller window.

we are only concerned with the overall level of the S_{11} parameter. Without the window, we see that the S_{11} parameter for the receiver meets our design goals. Also incorporated in Figure 4.5 is data about the rest of the UWB feed. One of the feed components, a hybrid combiner from Krytar, has been characterized at cryogenic temperatures. We used CST Microwave Studio to incorporate the receiver and combiner in a single circuit and measured their combined S_{11} parameters. The difference between the real data and the data generated by an ideal combiner in the software is shown in Figure 4.5. Although the reflection seems to increase slightly at higher frequencies, it still stays below -10 dB for the majority of the bandwidth.

Figure 4.6 shows the S_{11} parameters for the receiver with the window included. It is still better than -10 dB, and seems to be a little bit smoother than the S_{11} parameter without the window included. We see little change when comparing the ideal combiner to the real data, although we do see a slight increase in S_{11} at higher frequencies. In general, though, the S_{11} parameter still seems to be below or around -10 dB. It is important to note that the corrugated skirt was not included in the model for simulations where we calculated S_{11} parameters. The skirt should not affect the match of the receiver and it adds to the time it takes to complete simulations.

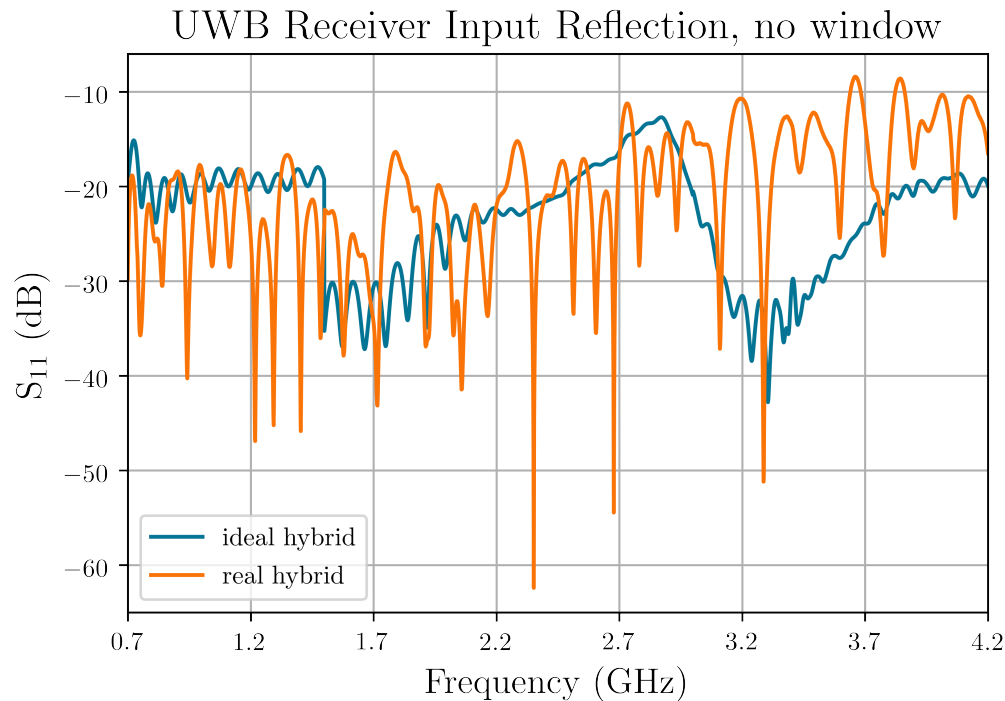


FIGURE 4.5: The S_{11} parameters for the UWB receiver with no window included in the model. Note that the S_{11} is better than -10 dB across the band.

The S_{11} parameters for the receiver are expected to improve for the final model with the smaller window and the addition of optimized Teflon matching layers. This is due to the smaller window size as well as the Teflon itself both acting to reduce return loss.

4.3 Measuring Window Strength

Because the window must withstand large forces due to the large vacuum pressure in the dewar, the fabrication of the window must include structural testing to the point of failure, also called destructive testing. In order to conduct these tests, an 8-inch diameter prototype version of the window was constructed. The prototype is shown in image (a) in Figure 4.7. During the testing process, the prototype is installed in the pressure vessel with the curved side facing inwards, as shown in image (b). A pressure gauge is installed near the apex of the window, a micrometer is added to measure window deflection with increasing pressure, and the pressure

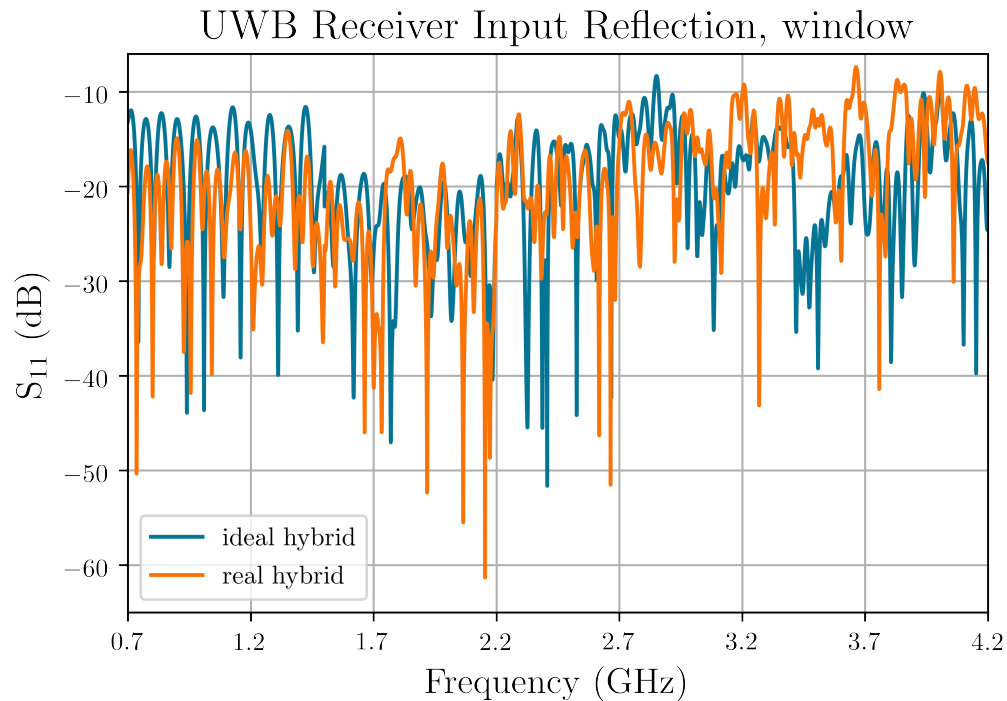


FIGURE 4.6: The S_{11} parameters for the UWB feed with the waveguide window. The S_{11} parameters are still better than -10 dB.

vessel is filled with water. The water is then pressurized until the window bursts. The same software used to design the window is used to determine the pressure at which the dome is expected to fail structurally. For this particular window, the pressure at which failure was expected was about 65 psi (Bob Simon, personal correspondence). For this test, the window burst at the expected pressure. The burst window can be seen in image (c) of Figure 4.7.

If the window is to be placed at the aperture of the receiver, its full diameter will be nearly 1 meter. To accommodate this possibility, Green Bank Observatory will use a spun metal dome as a mold for the larger window size. The metal dome is pictured in image (d) of Figure 4.7 and has been smoothed since the image was taken.



FIGURE 4.7: The UWB receiver waveguide window prototyping process. (a) shows the 8" diameter prototype of the window. (b) shows the prototype installed in the pressure vessel for testing. (c) shows the prototype after bursting. (d) shows a 40" diameter spun dome which will be the mold for the final window. Photos courtesy of Bob Simon at Green Bank Observatory.

CHAPTER 5: UWB Receiver Modal Excitation

5.1 Motivation for Mode Analysis

The feed efficiency reduction at 2.9 GHz due to a low phase efficiency, which was discussed in Section 3.3, can be mitigated by moving the detriment to a frequency at which a low efficiency is desirable. This is possible due to the phase efficiency's strong dependence on frequency. When the receiver is moved along the line of sight of the telescope, the phase center of the receiver moves with respect to the rest of the telescope. This moves the frequency detriment. A potential frequency to move the detriment to would be 2.4 GHz, at which a notch filter will already be used to excise radio-frequency interference from the SiriusXM satellite radio signal.

Even though the effect of the reduced efficiency at 2.9 GHz can be mitigated, its origin still sparks curiosity. All of the undesirable radiation pattern characteristics that stem from the UWB receiver's geometry are most likely related to the imbalance of higher-order waveguide mode excitation in the feed horn. [Beukman \(2015\)](#) presents a radio receiver design technique focused on understanding the waveguide modes which make up the receiver's radiation pattern. This modal makeup can, in theory, be used to determine the ideal parameters for the horn geometry without brute-force optimization. For a receiver which has already been designed, the first step of this process is to determine the modal makeup of the radiation pattern.

5.2 Circular Aperture Technique

A numerical method for determining the modal makeup of a receiver's radiation pattern was originally described by [Ludwig \(1965\)](#). An adaptation of this method utilized by [Beukman \(2015\)](#) and deemed the "circular aperture technique" was followed closely for this work using simulated far-field patterns from the UWB

receiver. The far-field pattern, F , of a receiver, which can be modeled as a waveguide with varying radius, is made up of a sum of electric fields excited by all modal components (Beukman 2015):

$$F(\rho, \phi) = \sum_{m=0, n=1}^{M, N} a_{mn} E^{TE_{mn}} + b_{mn} E^{TM_{mn}} \quad (5.1)$$

Here, a mode is specified using the indices m and n . $E^{TE_{mn}}$ and $E^{TM_{mn}}$ represent the transverse electric and transverse magnetic fields respectively at a radius ρ along the boresight of the receiver. The coefficients a_{mn} and b_{mn} represent the relative strengths of each mode. These coefficients are what we wish to calculate in order to determine the modal makeup of a far-field pattern.

At any position in a receiver, a far-field pattern should encode the modal breakdown of the radiation pattern at that point in the receiver. Similarly to the way Fourier analysis states that sinusoidal functions can represent any arbitrary function, the above representation of a far-field pattern should capture every possible pattern because the electric fields excited by waveguide modes form a complete set within a waveguide (Ludwig 1965). In order to determine the values of modal coefficients given a known far-field pattern, Ludwig (1965) solves for them algebraically. Beukman (2015) simplified them further, and we adapt them slightly below.

$$a_{mn} = -A_{mn} / (i^m k J_m(\chi'_{mn}) \chi_{mn}^2 a^2) \quad (5.2)$$

$$b_{mn} = B_{mn} / (i^m k J'_m(\chi_{mn}) \chi_{mn} a^2) \quad (5.3)$$

Here, i is the imaginary unit, $k = 2\pi/\lambda$ is related to the wavelength of the observation, J_m is the Bessel function of the first kind (order m) and $J_m(x)$ represents that Bessel function's value at some value x . J'_m represents the derivative of that Bessel function. Further, χ_{mn} is the n th zero of the Bessel function of the first kind of order m . Thus, χ'_{mn} is the n th zero of the derivative of that Bessel function. a

is the aperture radius. The remaining factors A_{mn} and B_{mn} are defined as follows.

$$A_{mn} = \frac{2}{1 + \sqrt{1 - \left(\frac{\chi'_{mn}}{ka}\right)^2}} \frac{2\chi'_{mn}}{\pi J'_p(\chi'_{mn})} \int_0^{2\pi} G_\phi(\chi'_{mn}, \phi) \sin(p\phi) d\phi \quad (5.4)$$

$$B_{mn} = \frac{2}{1 + \sqrt{1 - \left(\frac{\chi_{mn}}{ka}\right)^2}} \frac{2}{\pi J_{p+1}(\chi_{mn})} \int_0^{2\pi} G_\theta(\chi_{mn}, \phi) \cos(p\phi) d\phi \quad (5.5)$$

G_ϕ and G_θ are far-field patterns which can be simulated using a model of a receiver. They are defined at a specific azimuthal angle θ_i about the aperture, which are defined by $\theta_i = \sin^{-1}(\chi'_{mn}/(ka))$ for TE_{mn} modes and $\theta_i = \sin^{-1}(\chi_{mn}/(ka))$ for TM_{mn} modes. Within the integral, the far-field patterns are multiplied by a trigonometric function and then integrated along ϕ from one side of the aperture through the boresight and to the other side of the aperture.

5.3 Mode Analysis Results

We chose to calculate the modal breakdown in the aperture of the UWB receiver instead of in the throat because a cursory calculation revealed more higher-order modal excitation in the aperture. We used far-field patterns exported from our simulations at a variety of frequencies between 0.7 and 4.2 GHz. We compared the results for modal excitation for Models C and D to determine if the presence of the Teflon matching layers affected the modal content in the feed horn.

We focused on the modes TE_{11} , TE_{12} , TE_{13} , TM_{11} , TM_{12} , and TM_{13} . We expected our results to show excitation of higher-order TM modes (i.e. mainly TM_{13} and some TM_{12}) at around 2.9 GHz.

Our goal was to calculate the mode coefficients a_{mn} and b_{mn} at each frequency to determine the relative contribution to the radiation pattern of each TE_{mn} and TM_{mn} mode respectively. This process involved first exporting far-field patterns G from our simulation at the appropriate azimuthal angle θ_i as specified in the previous sub-section. Then, a Python script was used to calculate the values of the factors A_{mn} or B_{mn} depending on whether we were calculating a coefficient

for a TE mode or a TM mode. The script finished by calculating the final mode coefficients a_{mn} and b_{mn} .

Once all of the coefficients in our analysis were calculated for each frequency (i.e. a_{11} , a_{12} , a_{13} , b_{11} , b_{12} , and b_{13}), we calculated the percent contribution of each coefficient at that frequency. We present the results of our modal excitation analysis of the UWB receiver here. Figure 5.1 shows the contribution of each of the modes at a given frequency to the far-field pattern of Model C of the receiver at that frequency. As anticipated, the TE₁₁ mode is dominant in the aperture at the lowest frequencies. Its dominance decreases at around 2.7 GHz, and higher-order modes like TM₁₂ and TM₁₃ begin to have more influence at around 3.5 GHz. Thus, a correlation exists between decreased efficiency performance and higher-order mode generation. However, this is not as extreme as we predicted.

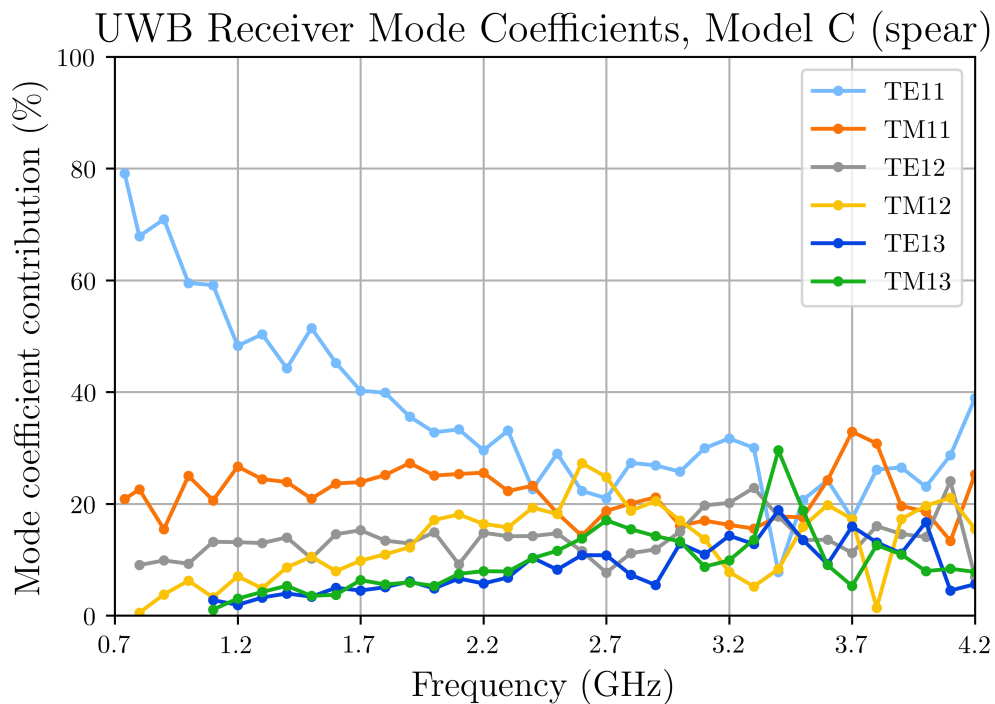


FIGURE 5.1: Modal makeup of the UWB receiver radiation pattern as a function of frequency for Model C, which includes the dielectric spear but no Teflon matching layers. As expected, the TE₁₁ mode dominates at lower frequencies, but higher order modes like TM₁₂ and TM₁₃ gain power at around 3.5 GHz.

We also calculated the modal excitation in the aperture for Model D, which included the Teflon matching layers. As we reported in Section 3.3, the addition of the Teflon matching layers seemed to solve the issue of greatly decreased phase efficiency at around 2.9 GHz. Therefore, one might anticipate that the solution to that issue might cause some large change in the modal content in the horn which dictates the radiation pattern. We present the modal breakdown for Model D in Figure 5.2. If we compare Figures 5.1 and 5.2, we notice no significant difference between mode excitation as a function of frequency except for a very slight increase in TE_{11} excitation at high frequencies. The percent contribution of each mode remains generally in the same order as we move from a large dominance to a small dominance, save some randomness at higher frequencies. This indicates that the addition of Teflon matching layers does not severely impact the actual relative modal content in the feed horn, but instead alters the phase velocities of the modes relative to each other, which improves the shape of the radiation pattern.

This modal analysis is still a work in progress. As we continue to iterate through models and optimize components of the UWB receiver, we may repeat this analysis to see if there are any measurable changes in the predicted modal content of the feed horn.

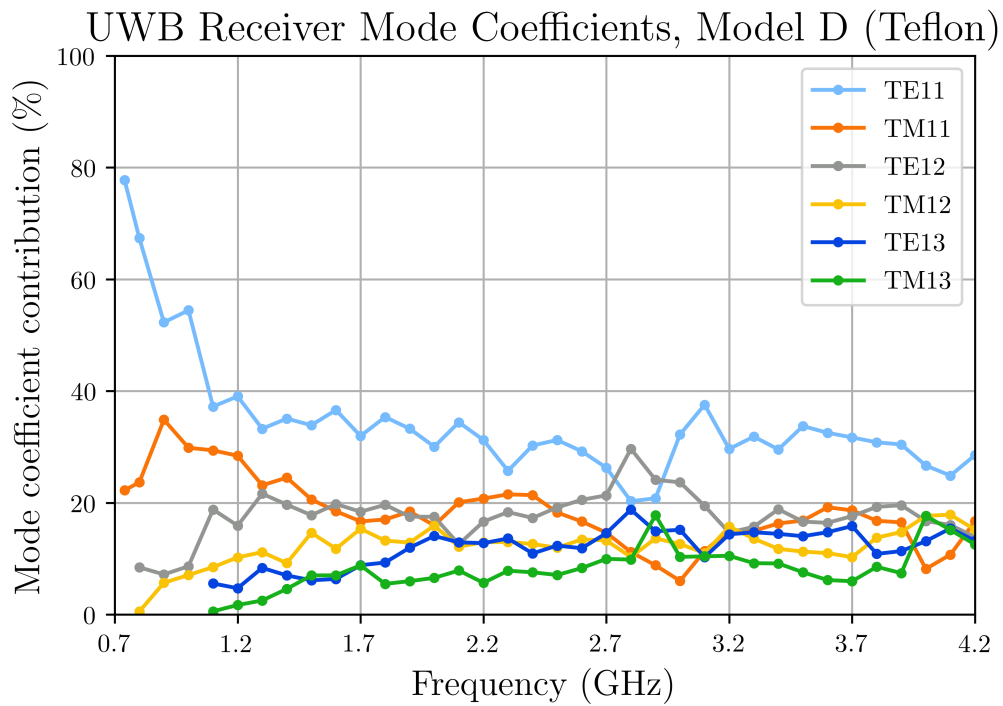


FIGURE 5.2: Modal makeup of the UWB receiver radiation pattern as a function of frequency for Model D, which includes the Teflon matching layers. There is no significant difference between the modal breakdown for Models C and D except for slightly more excitation of TE₁₁ at high frequencies for the latter model.

CHAPTER 6: Conclusions and Future Work

The Green Bank Telescope ultra-wideband receiver meets design goals in its current state, although some further optimization is needed to perfect the design. At lower frequencies, the total feed efficiency seems to be around 60% for most of our models. The quartz dielectric insert improves efficiency performance at high frequencies, and the Teflon matching layers reduce the effect of phase errors in the aperture at around 2.9 GHz, so further adjustments to the dimensions of the Teflon layers should bring the total receiver efficiency to above 50% at higher frequencies. Prototypes of the waveguide window show promising results for its ability to withstand the required vacuum pressure within the receiver, and simulations of the window indicate that its curved geometry will not affect signal reflection significantly (the S_{11} parameters of the receiver with the window are below -10 dB across the receiver bandwidth).

The addition of lossy Teflon matching layers to the UWB receiver model improves the efficiency detriment we initially noticed. However, it brings the total efficiency down at higher frequencies. This may be able to be improved by optimizing certain aspects of the matching layer design. The overall shape of the solid Teflon and grooved Teflon layers can be optimized to maximize efficiency, and the groove thickness and depth can also be changed. Work on this optimization will continue. However, above 3.5 GHz, the flux of most pulsars which will be observed using this receiver rolls off anyway (Steve White, personal correspondence). The larger concern is the impact on the S_{11} parameters due to the inclusion of the Teflon dielectric material.

Our waveguide mode analysis of the receiver with the Teflon matching layers included shows that higher-order mode excitation occurs at higher frequencies. However, we cannot conclude that the higher-order mode excitation causes the dip in efficiency that we initially observed at 2.9 GHz, as the addition of Teflon matching layers seems to fix this efficiency detriment but cause little change in the modal makeup in the aperture of the receiver. Future work in the exploration of modal excitation in the UWB receiver may include calculation of mode coefficients for modes of even higher order (for instance, [Beukman \(2015\)](#) explores TE_{31} and

TE₃₂), though this will likely only be performed out of curiosity rather than for further optimization of the receiver.

The UWB receiver project will continue its development at Green Bank for the rest of 2020 and into 2021. As of April 2020, mechanical drawings for the components of the receiver have been completed and sent to the machine shop. The first ridge has been fabricated and the next component to be fabricated will be the flared feed horn itself. On the software side of the receiver development, an extension of the existing backend for another GBT receiver, the Versatile GBT Astronomical Spectrometer (VEGAS), is underway, which will help support the backend for the UWB receiver.

Once fabrication of the receiver is complete, some of the predictions we made using simulated models of the receiver can be confirmed. For instance, actual co-polar and cross-polar radiation patterns can be measured, as well as the S_{11} parameters across the bandwidth (Dunning et al. 2015). The total noise temperature of the receiver can also be measured once it is installed on the telescope, allowing us to test our estimates of spillover noise temperature.

The development of this UWB receiver for the GBT will ensure that the telescope remains a premier instrument for pulsar timing moving into the future. A detection of nanohertz-frequency gravitational waves using pulsar timing with the GBT would represent a significant step forward in improvements in receiver sensitivity and open the door to countless scientific endeavors harnessing these benefits. Because of these improvements, pulsar timing is predicted to be able to detect gravitational waves within the next five years (Condon & Ransom 2016). Only about 50 years after their discovery by Jocelyn Bell Burnell (Hewish et al. 1968), pulsars are being used as invaluable tools in the pursuit of a new frontier for observational astronomy. Building a sensitive enough radio receiver to understand them is just one important piece in the greater puzzle.

This project was funded by the National Science Foundation through the Research Experience for Undergraduates program at the Green Bank Observatory. The Green Bank Observatory is a facility of the National Science Foundation operated under cooperative agreement by Associated Universities, Inc.

Bibliography

- Abbott, B. P., Abbott, R., Abbott, T. D., et al. 2016, *Phys. Rev. Lett.*, 116, 061102
- Akgiray, A. H. 2013, California Institute of Technology, doi:10.7907/TYX5-2C48
- Armano, M., Audley, H., Auger, G., et al. 2016, *Phys. Rev. Lett.*, 116, 231101
- Beukman, T. S. 2015, Stellenbosch University
- Beukman, T. S., Meyer, P., Ivashina, M., & Maaskant, R. 2016, *IEEE Transactions on Antennas and Propagation*, 64, doi:10.1109/TAP.2016.2537363
- Carroll, B. W., & Ostlie, D. A. 2017, *An Introduction to Modern Astrophysics* (Cambridge University Press)
- Collin, R. 1984, *IEEE Transactions on Antennas and Propagation*, 32, 997
- Condon, J. J., & Ransom, S. M. 2016, *Essential Radio Astronomy* (Princeton University Press)
- Dunning, A., Bowen, M., Bourne, M., Hayman, D., & Smith, S. L. 2015, in 2015 IEEE-APS Topical Conference on Antennas and Propagation in Wireless Communications (APWC), 787–790
- Griffiths, D. J. 2013, *Introduction to Electrodynamics*, 4th edn. (Pearson Education, Inc.)
- Hewish, A., Bell, S. J., Pilkington, J. D. H., Scott, P. F., & Collins, R. A. 1968, *Nature*, 217, 709
- Johnson, R. C. 1993, *Antenna Engineering Handbook* (McGraw-Hill Education)
- Kildal, P.-S. 1985, *IEEE Transactions on Antennas and Propagation*, 33, 903
- Lam, M. T., Cordes, J. M., Chatterjee, S., & Dolch, T. 2015, *ApJ*, 801, 130
- Laverghetta, T. S. 1976, *Microwave Measurements and Techniques* (Artech)

Bibliography

46

- Lorimer, D. R., & Kramer, M. 2005, Handbook of Pulsar Astronomy (Cambridge University Press)
- Ludwig, A. 1973, IEEE Transactions on Antennas and Propagation, 21, 116
- Ludwig, A. C. 1965, Space Programs Summary 37-26, vol. IV, 200-208
- Moore, C., Cole, R., & Berry, C. 2019, Gravitational Wave Detectors and Sources
- NANOGrav Collaboration, Arzoumanian, Z., Brazier, A., et al. 2015, ApJ, 813, 65
- Norrod, R., & Srikanth, S. 1996, GBT Memo 155
- Roshi, D. A., Anderson, L. D., Araya, E., et al. 2019, Astro2020 Activities and Projects White Paper: Arecibo Observatory in the Next Decade, arXiv:1907.06052
- Simon, R. J. 2005, NRAO Electronics Division Internal Report 315